ETH zürich

ETH Library

# $CO_2$ splitting via a solar thermochemical cycle based on Zn/ZnO redox reactions: thermodynamic and kinetic analysis

**Master Thesis**

**Author(s):**
Hischier, Illias

**Publication date:**
2008

**Permanent link:**
https://doi.org/10.3929/ethz-a-005565519

**Rights / license:**
In Copyright - Non-Commercial Use Permitted

This page was generated automatically upon download from the ETH Zurich Research Collection.
For more information, please consult the Terms of use.

**Swiss Federal Institute of Technology Zurich ETHZ**

# $CO_2$ splitting via a solar thermochemical cycle based on Zn/ZnO redox reactions: Thermodynamic and kinetic analysis

**Illias Hischier**

**Master Thesis**

**January 2008**

**Dr. Elena Gálvez**

**Prof. Aldo Steinfeld**

**Professorship in Renewable Energy Carriers**

**Institute of Energy Technology**

# Abstract

A novel $CO_2$ splitting cycle via Zn/ZnO redox reactions is proposed. Based on concentrated solar power it allows the production of renewable fossil fuels. The cycle is theoretically examined by 1st law, 2nd law and thermo-economic analysis. In addition, exergy efficiencies were determined for different scenarios. A kinetic study of the oxidation of zinc with $CO_2$ at 623 – 823 K and ambient pressure has been performed in a thermogravimeter system. The formation of hollow ZnO shells has been observed and a growth mechanism is proposed. Based on the shrinking core model an apparent activation energy of 96.1-148.1 kJ/mol, depending on $CO_2$ partial pressure, has been found. A reactor study was performed in an aerosol flow reactor. At a $CO_2$:Zn(g) stoichiometry of 1, an optimum of 39% was found for both, Zn to ZnO conversion and $CO_2$ to CO conversion. For optimization, a rotary counter flow reactor is proposed which benefits from the advantageous ZnO shell formation.

# Acknowledgments

I would like to thank Aldo Steinfeld, Professor for Renewable Energy Carriers at the Swiss Federal Institute of Technology in Zurich for giving me the opportunity to take part in this new and very interesting project.

My thanks go furthermore to Dr. Elena Gálvez for supervising this project and for her helpful support. I could profit a lot from her knowledge and her inputs and our discussions that were always very constructive.

Special thanks go to Alwin Frei at the PSI for support in the experimental analysis and Peter Loutzenhiser for discussing the theoretical analysis.

Last but not least my thanks go to Philipp Haueter and Gustavo Lunardi for helping me in carrying out the laboratory work.

# Table of contents

# 1 Introduction

## 1.1. Global climate change and the $CO_2$-problem

One of the main problems confronting mankind today is the global climate change with its tremendous consequences predicted for the mid-term future of the next 20-30 years. There is much evidence and high agreement about the fact that human activities have led to a marked increase in atmospheric global greenhouse gas (GHG) concentration contributing to higher global temperatures and thus to the climate change. Thereby, carbon dioxide is the most important anthropogenic greenhouse gas [1]. Since the mid-19$^{th}$ century over 1100 $GtCO_2$ have been released into the atmosphere. The trend towards increasing $CO_2$ concentration in the atmosphere has temporarily been stopped by the two oil crises 1973 and 1979. Since then, all fossil fuel options responsible for $CO_2$ emissions have continued to be fully used.

Today, about 85% of global $CO_2$ emissions produced annually result from the combustion of fossil fuels supplying 80% of world's primary energy demand. However, $CO_2$-emissions at current or increasing rates due to the extraction and combustion of oil, coal and natural gas are no longer environmentally acceptable. Facing global climate change a sustainable energy future, i.e. a transition to zero- and low-carbon sources for energy production has to be achieved as soon as possible. Existing infrastructures and energy conversion technologies are still mainly based on carbon containing fuels and hence such a transition requires huge investments in new infrastructures as well as in research and development (R&D).

The most effective way to stop the trend towards increasing $CO_2$-concentration in the atmosphere is to maximize utilization of energy sources by using technologies with the highest efficiency available. Key mitigating technologies proposed beside improved supply and distribution efficiency for the solution of the $CO_2$-problem are nuclear energy technologies, carbon dioxide capture and storage (CCS) and technologies based on renewable energy. The past has shown that no single technology is able to overcome the fossil burden as every technology has its drawbacks. Nuclear energy has been exhibiting local and regional environmental deficiencies such as risks of radiation leakage, harmful waste and other constraints (e.g. weapon proliferation). CCS technologies currently developed lack of long-term liability associated with the leakage of $CO_2$ to the atmosphere and unpredictable local environmental impacts. Finally, renewable energy sources are mostly widely dispersed and variable over hourly, daily and/or seasonal time frames. They hence must be used either in a distributed manner or concentrated and made transportable to meet the higher energy demands of cities and industries. Energy-storage technologies have therefore become a major concern for successful the implementation of renewable energies.

## 1.2. Concentrating solar power for thermochemical cycles

Solar energy is the primary energy source on our planet's surface. The proportion of solar radiation that reaches the Earth's surface is more than 10'000 times the current annual global energy consumption [1]. In other words, the Earth receives from the sun each hour as much energy as mankind consumes in a year. The drawbacks are, as already mentioned, well-known: the solar radiation reaching the earth is very dilute (only about 1 $kW_{th}/m^2$), intermittent and unequally distributed over the surface of the earth (mostly between 30° north and 30° south latitude) [2]. An ideal solution to overcome these barriers is the use of concentrated solar power (CSP) technologies to run a thermochemical reaction. The basic idea is to concentrate the diluted sunlight by parabolic mirrors in order to obtain heat at high temperatures for driving a chemical transformation and store the solar energy in fuels which are easily transportable and hence allow a worldwide time independent distribution of solar energy.

The simplest way to produce solar fuels would be by single-step (direct) solar reduction processes such as the thermal water dissociation for the production of hydrogen [3] or direct reduction of $CO_2$ to fuel [4]. Although these processes are conceptually simple they are impeded by the need to use very high temperatures and an effective technique for separating the gaseous products at theses high temperatures to avoid recombination and ending with an explosive mixture. Therefore, recently several solar thermochemical cycles have been proposed. They do not only bypass the separation problem but also lower the operating upper temperatures, which facilitate the selection of appropriate materials for the reactors involved. A selection of such thermochemical cycles is given in [5]. In general, the most efficient cycles consist of two steps: In a first endothermic reaction a metal oxide such as zinc oxide or iron oxide is thermally reduced by using concentrated solar power. The concentrated solar energy is then stored as chemical energy and available for storage, transport or further energy conversion. In a second exothermic step the metal is transformed back into its initial state by oxidation and thereby releasing the stored solar energy for further use. By recycling the metal oxide to the first step the cycle is closed and a continuous operation is possible with a finite amount of metal oxide acting as energy carrier.

## 1.3. $CO_2$-splitting cycle

In this study the possibility of using a solar thermochemical cycle for $CO_2$-decomposition will be explored. The $CO_2$-splitting via a thermochemical cycle based on CSP enables the production of solar fossil fuels, carbon monoxide or solid carbon, which are "$CO_2$-neutral". These fuels would represent an excellent mid-term solution of the $CO_2$-problem by building a bridge between energy technologies and infrastructures still largely based on fossil fuels today and technologies and infrastructures based on renewable energy in the future. They will facilitate the transition into a sustainable energy future not only in the industrialized world, but also in newly industrializing countries such as China and India. Furthermore, the conversion of gaseous $CO_2$ into solid carbon by using solar energy would be a sustainable and safe method for $CO_2$ sequestration.

Ecological reasons such as energy security and air quality will certainly not be sufficient to convince governments in many developing countries to adopt policies favouring such a solution. It

will therefore also have to be demonstrated that the proposed solution is not only affordable, but that it will be, due to its saving potential, key to the future economic development of the societies concerned. In other words, it may become viable for governments to reduce $CO_2$-emissions not only due to ecological reasons, but also due to economic reasons.

For the reduction of $CO_2$ the following novel two-step cycle is proposed:

$$1^{st}\text{ step:} \qquad M_xO_y \rightarrow xM + \frac{1}{2}yO_2 \tag{1.1}$$

$$2^{nd}\text{ step a):} \qquad xM + yCO_2 \rightarrow M_xO_y + yCO \tag{1.2}$$

$$\text{or} \qquad 2^{nd}\text{ step b):} \qquad xM + \frac{1}{2}yCO_2 \rightarrow M_xO_y + \frac{1}{2}yC \tag{1.3}$$

M denotes the metal and $M_xO_y$ the corresponding metal oxide. In the cycle, the metal serves as an energy carrier, saving solar energy in the first step and releasing it in the second by reducing $CO_2$ to form carbon monoxide or solid carbon. After the second step, the metal is recycled to the first step again. Thus the net reaction is $CO_2 \rightarrow CO + 1/2\,O_2$ or $CO_2 \rightarrow C + O_2$. Among the possible redox pairs suitable for the proposed cycle are Zn/ZnO, FeO/$Fe_3O_4$ and Mg/MgO. In this thesis Zn/ZnO is considered for the theoretical and experimental study. It has already been identified as one of the most favourable candidate metal redox pair for the similar 2-step water splitting cycle [6]. Since several thermochemical aspects have already been studied extensively the achievements of the first step, which is identical to the here proposed cycle, can be adopted here. The focus of the present study will be on the new second step, the reaction of Zn and $CO_2$ in a $CO_2$-reactor. An exemplary scheme of the $CO_2$-splitting cycle using zinc is given in Fig. 1-1 for the production of carbon monoxide and in Fig. 1-2 for the production of solid carbon.

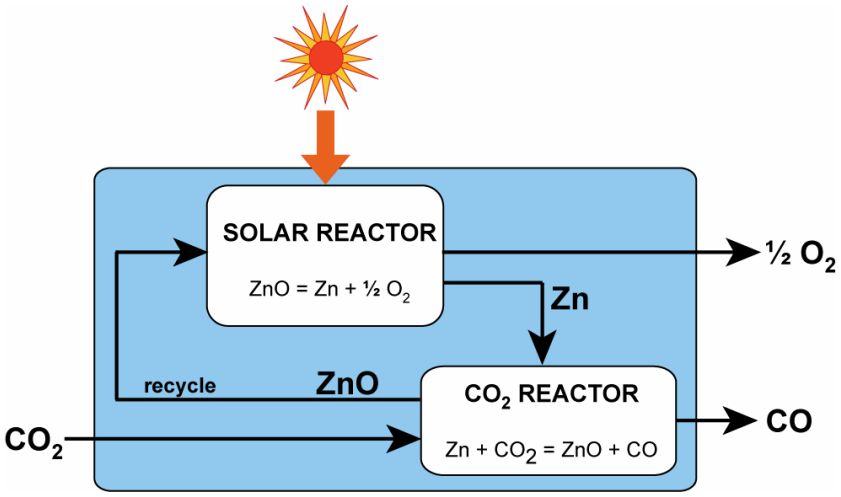


Fig. 1-1: Scheme of the CO2 reduction to CO with zinc

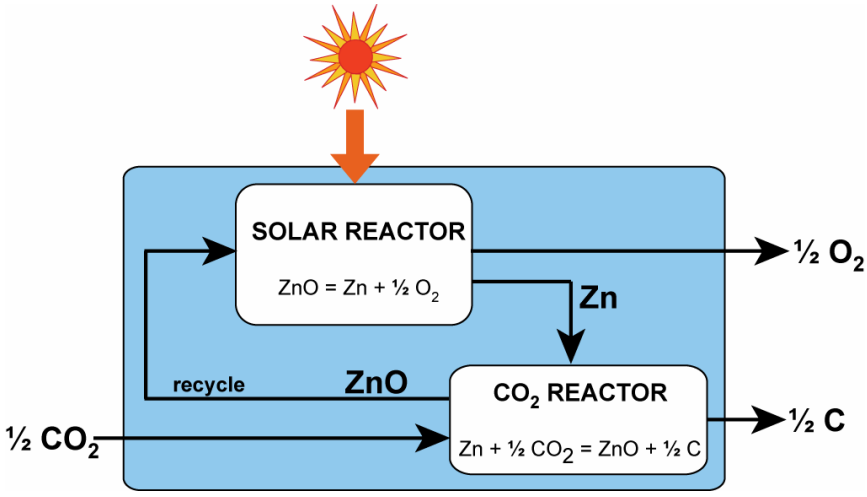


Fig. 1-2: Scheme of the $CO_2$ reduction to solid C with zinc

# A. Theoretical Analysis

# 2 Literature Review

The first step, the reduction of zinc oxide has already been well investigated by several researchers mainly in connection with the 2-step water-splitting thermochemical cycle. A scientific framework is given by Palumbo et al [7]. A chemical equilibrium study revealed that ZnO is essentially decomposed into the products Zn(g) and $O_2$ above 2000 K. Furthermore, decomposition and subsequent quench for separation of the gaseous products were effected in a solar furnace and in a solar furnace simulator. Zn yields as high as 90% have been achieved. A novel solar chemical reactor for conducting the thermal dissociation of ZnO at above 2000 K was presented by Haueter et al. [8]. The reactor features a windowed rotating cavity-receiver lined with ZnO particles that are held by centrifugal forces. An improved version of the reactor was designed and built by Müller et al. [9] and experimentally tested for both the thermal reduction of ZnO(s) and the carbothermal reduction of the oxide. For the carbothermal reduction the solid product was zinc with a purity exceeding 95%mol. However, the thermal decomposition lacks of high Zn yield due to insufficient quench rates and recombination processes. Further research is needed to overcome this problem. Recently, in the framework of the EU-project SOLZINC, a 300 kW solar chemical pilot plant for the carbothermal production of zinc was experimentally demonstrated [10]. The solar chemical reactor was batch-operated in the 1300-1500 K range and yielded 50 kg/h of 95%-purity Zn. The measured energy conversion efficiency (ratio of reaction enthalpy change to the solar power input) was 30%.

About the second step, the reduction of $CO_2$ using Zn as reducing agent, only little experimental data have been found, although, for the first time this reaction has been proposed already in 1980 by Martin [11]. Most literature dealing with the oxidation of Zn in the presence of $CO_2$ are related to the Imperial Smelting Process and study the oxidation of zinc vapour in CO-$CO_2$ mixtures. An overview and comparison of past literature is given by Lewis and Cameron [12]. They reported the oxidation of gaseous Zn to ZnO while $CO_2$ is reduced to CO at temperatures between 1073 and 1273 K. Furthermore, they found small quantities of carbon deposits indicating that some CO was further reduced to C in the presence of gaseous Zn. However, Cox and Fray [13], who did similar experiments, however claimed, that possible carbon depositions were caused by sulphur contamination and CO is not a viable species for oxidising zinc. Other attempts to reduce $CO_2$ have been carried out with wustite [14-16], oxygen-deficient magnetite [17, 18] or magnesium [19].

In the following chapters the $CO_2$ splitting to CO or C is investigated by thermochemical equilibrium-, 2$^{nd}$ law- and economic-analysis.

# 3 Thermodynamic analysis

The first step, the thermal dissociation of ZnO, is an endothermic reaction with a standard enthalpy change of reaction of 350.5 kJ/mol (eq. (3.1)). In the temperature range of interest, ~2300 K [20], apparent activation energies of 312-376 kJ/mol have been reported [21, 22].

$$1^{st}\text{ step:} \qquad ZnO \rightarrow Zn + \frac{1}{2}O_2 \qquad \Delta H^0_{298K} = 350.5\ kJ \cdot mol^{-1} \qquad (3.1)$$

The second step, the reaction of zinc with $CO_2$, is exothermic and showing a standard enthalpy change of reaction of -67.5 kJ/mol when reducing $CO_2$ to CO (reaction 2a, eq. (3.2)) and -153.7 kJ/mol when reducing $CO_2$ completely to C (reaction 2b, eq. (3.3)). Theoretically, the energy released during the exothermic reaction is sufficient to heat up the reactants to a reaction temperature of 1070 K and 2785 K for reaction 2a and reaction 2b, respectively.

$$2^{nd}\text{ step a):} \qquad Zn + CO_2 \rightarrow ZnO + CO \qquad \Delta H^0_{298K} = -67.5\ kJ \cdot mol^{-1} \qquad (3.2)$$

$$2^{nd}\text{ step b):} \qquad Zn + \frac{1}{2}CO_2 \rightarrow ZnO + \frac{1}{2}C \qquad \Delta H^0_{298K} = -153.7\ kJ \cdot mol^{-1} \qquad (3.3)$$

Thermochemical equilibrium calculations have been performed using HSC Outokumpu program code [23]. Product species with mol fractions less than $10^{-5}$ have been omitted.

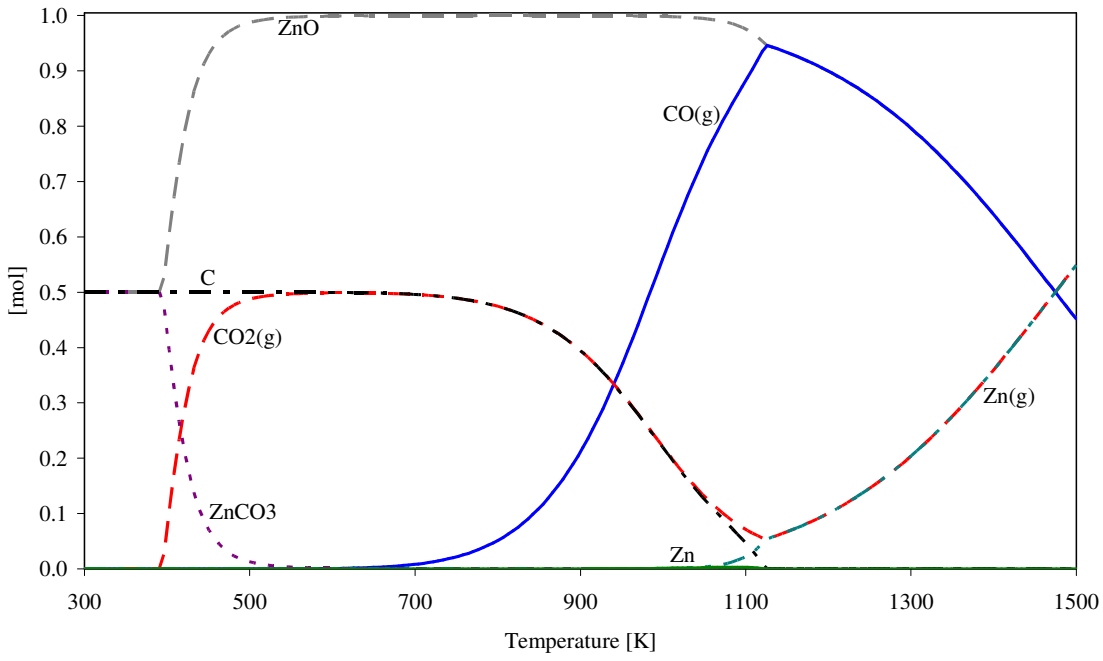


Fig. 3-1: Equilibrium composition of the system Zn + $CO_2$ (reaction 2a) as a function of temperature at 1 bar.

Fig. 3-1 shows the equilibrium composition of 1 mol zinc reacting with 1 mol $CO_2$ (reaction 2a) as a function of temperature in the range of 300 – 1500 K at 1 bar. The temperature of interest, where Zn is completely converted to ZnO, lies between 570 and 1000 K. Below 570 K the formation of zinc carbide may occur and above 1000 K CO starts to reduce ZnO to gaseous zinc. Depending on the desired product, gaseous CO or solid C, different temperatures are of interest: C yield reaches maximum below 700 K, while CO yield peaks at 1130 K. The decrease of C above 700 K is in agreement with the Boudouard reaction, eq. (3.4), which is well-known from the iron industry. As it can be observed from the Boudouard equilibrium (Fig. 3-2), C is oxidized to CO in the presence of $CO_2$ above ~700 K.

$$\frac{1}{2}CO_2 + \frac{1}{2}C = CO \qquad (3.4)$$

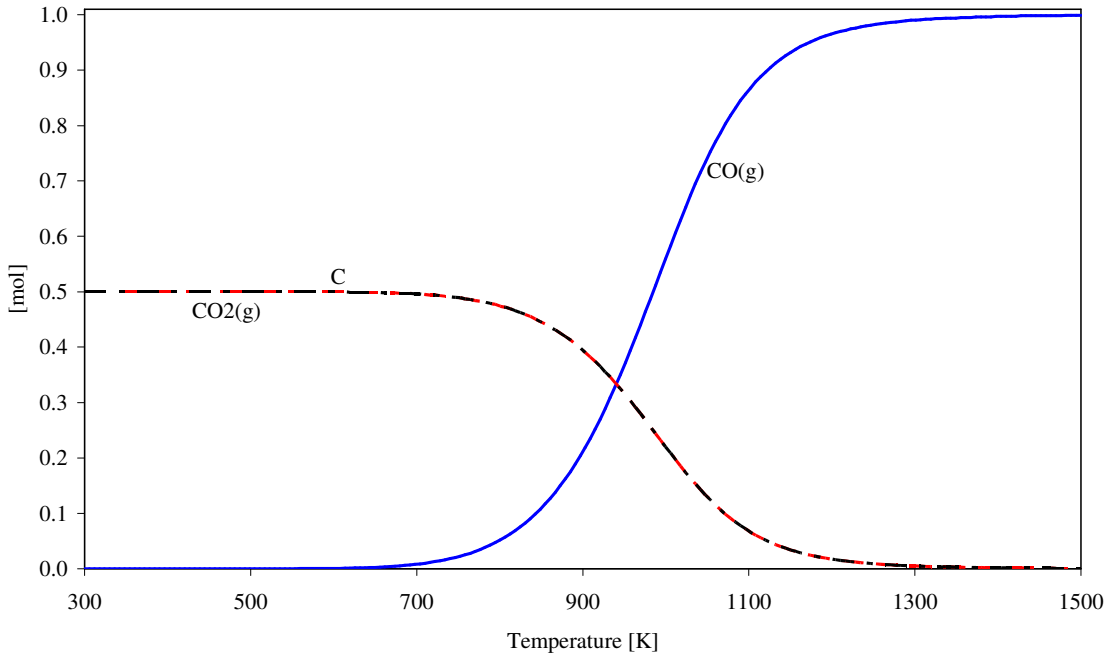


Fig. 3-2: Boudouard equilibrium as a function of temperature at 1 bar.

Regarding the equilibrium composition calculations one has to keep in mind that real equilibrium is reached only after infinite time and in a closed reaction cell. As we are looking at a time restricted reaction in an open reactor and gaseous products will be removed continuously, the final composition may be different from the one expected according to equilibrium composition. E.g. any condition leading to the production of CO (according to the Boudouard equilibrium traces of gaseous CO can be found at above 400 K) may shift the Boudouard reaction to the right. If at the same time the product, gaseous CO, is removed, the reaction will proceed until one of the educts will be consumed up completely, in this case C, thus making the production of carbon impossible. In other words, in an open reactor, the production of C is only favourable if the molar rate of $CO_2$ is equal or smaller than the one of zinc, as it is the case in reaction 2b (eq.(3.3)).

Fig. 3-3 shows the equilibrium composition of 1 mol zinc and 0.5 mol $CO_2$ (reaction 2b) as a function of temperature in the range of 300 – 1500 K at 1 bar. Below 1000 K, $CO_2$ is completely decomposed to C and zinc fully converted to zinc oxide. Above 1000 K, ZnO is carbothermally reduced, forming Zn, CO and $CO_2$. Hence complete reduction of $CO_2$ to C is only possible at a temperature below 1000K.

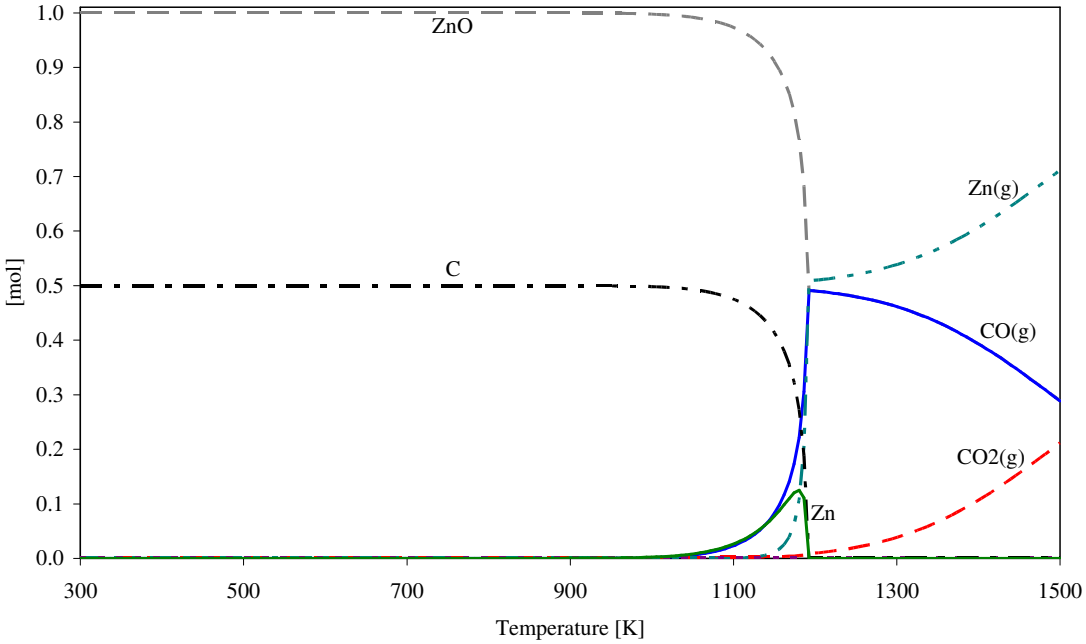


Fig. 3-3: Equilibrium composition of the system Zn + 0.5$CO_2$ (reaction 2b) as a function of temperature at 1 bar.

The reaction extents for CO and for C are defined according to equations (3.5) and (3.6).

$$X_{CO} = \frac{n_{CO}^{eq.}}{n_{Zn}} \tag{3.5}$$

$$X_{C} = \frac{n_{C}^{eq.}}{0.5 \cdot n_{Zn}} \tag{3.6}$$

$n_{CO}^{eq.}$ and $n_{C}^{eq.}$ are the number of moles CO and C in the equilibrium composition for a given temperature and pressure. $n_{Zn}$ is the total number of moles zinc available for the reaction and equivalent to the maximum achievable number moles CO or two times the number of moles C, respectively.

The reaction extents for reaction 2a and 2b are given in Fig. 3-4 and Fig. 3-5 as a function of temperature at 0.1, 1 and 10 bar. An increase in pressure shifts the shape of the reaction extent to higher temperatures. For a given temperature this results in a reduction of the CO reaction extent and in an increase of the C reaction extent. E.g., for reaction 2a, at 900 K, an increase from 1 to 10 bar reduces the CO yield form 21% to 7% and increases the C yield from 79% to 93%. Hence, at higher pressure, the production of C is favoured over the production of CO. This is in accordance with Le Chatelier's principle predicting the preference of the reaction leading to smaller volume

when increasing the pressure. As it can be seen in Fig. 3-5, an increase in pressure allows furthermore the production of solid carbon at higher temperatures. While at 1 bar full conversion to C is only favourable below 1000K, at a higher pressure of 10 bar full conversion is possible up to 1100 K.

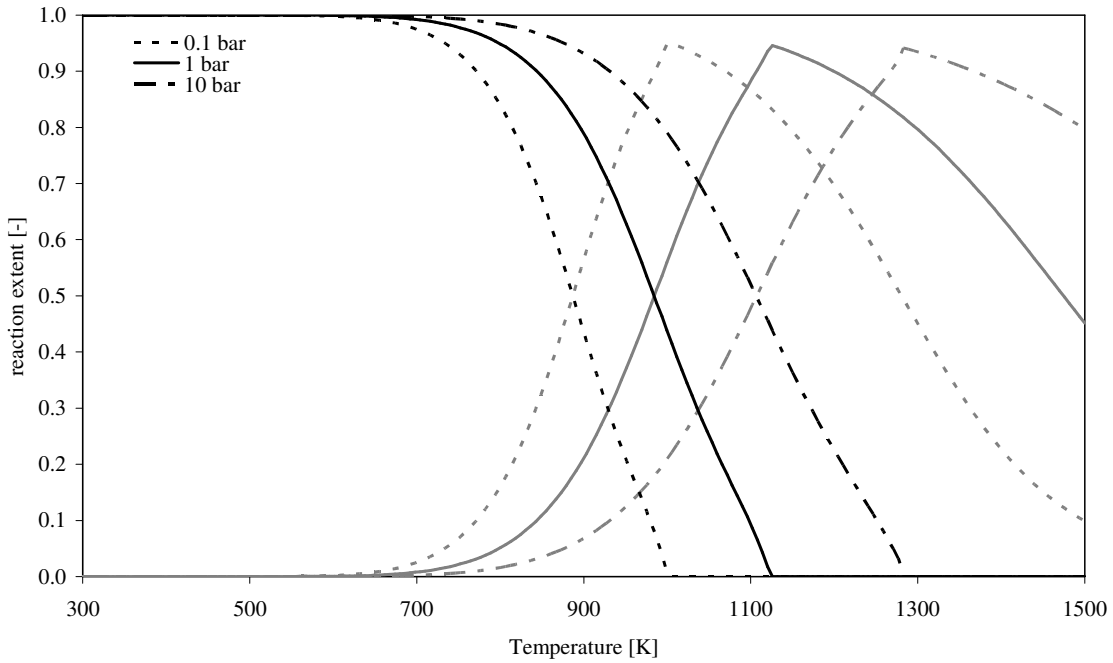


Fig. 3-4: Reaction extent of carbon, $X_C$ (black line), and carbon monoxide, $X_{CO}$ (grey line) for reaction 2a as a function of temperature at 0.1, 1 and 10 bar.

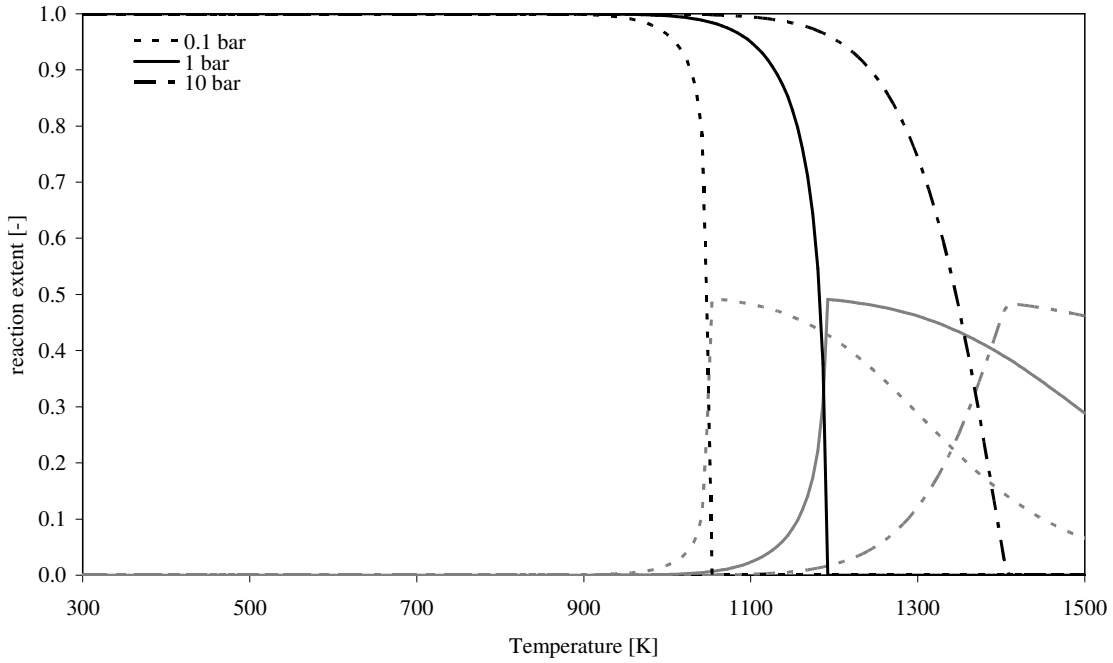


Fig. 3-5: Reaction extent of carbon, $X_C$ (black line), and carbon monoxide, $X_{CO}$ (grey line) for reaction 2b as a function of temperature at 0.1, 1 and 10 bar.

Fig. 3-6 shows the enthalpy change $\Delta H$ of reactions 2a and 2b as a function of temperature and at ambient pressure. The enthalpy change (eq.(3.7)) is defined for reactants fed at ambient temperature (298 K) and products obtained at the reaction temperature T and having an equilibrium composition as given in Fig. 3-1 and Fig. 3-3 for reaction 2a and 2b, respectively.

$$\Delta H = H_{\mathrm{T}}^{\text{products in equilibrium}} - H_{298K}^{\text{reactants}} \tag{3.7}$$

The enthalpy change is not only indicating the process heat required for the chemical transformation but also the sensible heat needed to heat the reactants from ambient to the reaction temperature which is indicated by the steady increase of the curves. The change in the slope of reaction 2a at ~400 K corresponds to the decomposition of $ZnCO_3$ and beginning of ZnO formation. Above 700 K the steady slope increase is indicating the production of CO due to a shift in the Boudouard equilibrium. Finally, at ~1100K where the reaction turns endothermic, a final change in the slope can be observed due to the carbothermal reduction of ZnO in the presence of CO and formation of gaseous Zn. Reaction 2b shows only one increase in the slope of its enthalpy change between 1100-1200 K due to the carbothermal reduction of ZnO to gaseous Zn.

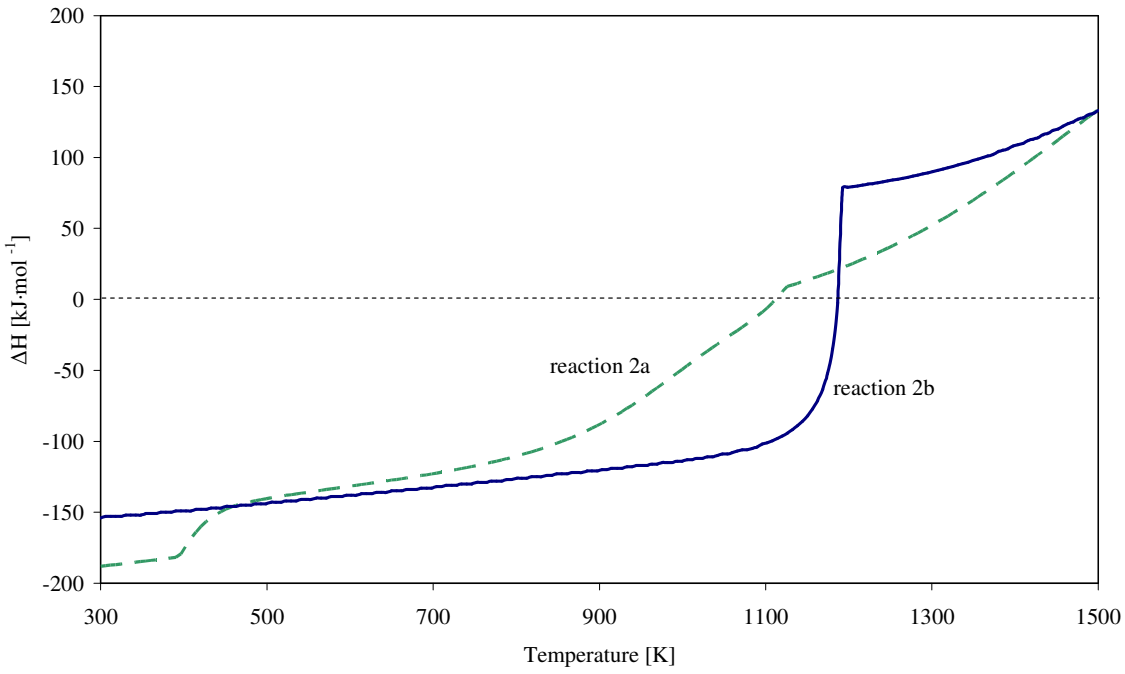


Fig. 3-6: Enthalpy change as a function of temperature for the reactions 2a and 2b at 1 bar.

# 4 2nd law analysis

## 4.1. Solar-to-chemical energy conversion efficiency

Based on the derivation of Steinfeld [20] a 2nd law (exergy) analysis is performed to establish the maximum exergy efficiency of the proposed 2-step cycle. The exergy efficiency is an important criterion for judging the relative industrial potential of the proposed cycle compared to various other solar-thermal chemical processes. It measures how well the solar energy $Q_{solar}$ is converted into chemical energy $\dot{n}\Delta G_{products}$ (eq. (4.1)). The chemical energy is thereby defined as the maximum possible amount of work that can be extracted from the products when transformed back to reactants at 298K and is given by the change in gibbs free enthalpy times the molar flow $\dot{n}$. It is hence equal to the work of a reversible, ideal fuel cell.

$$\eta_{exergy} = \frac{-\dot{n}\,\Delta G_{products}\big|_{298K}}{Q_{solar}} = \frac{W_{FC,ideal}}{Q_{solar}} \tag{4.1}$$

The proposed $CO_2$-splitting cycle is represented by the model flow diagram in Fig. 4-1. It comprises a solar reactor, a quench unit and a $CO_2$ reformer.

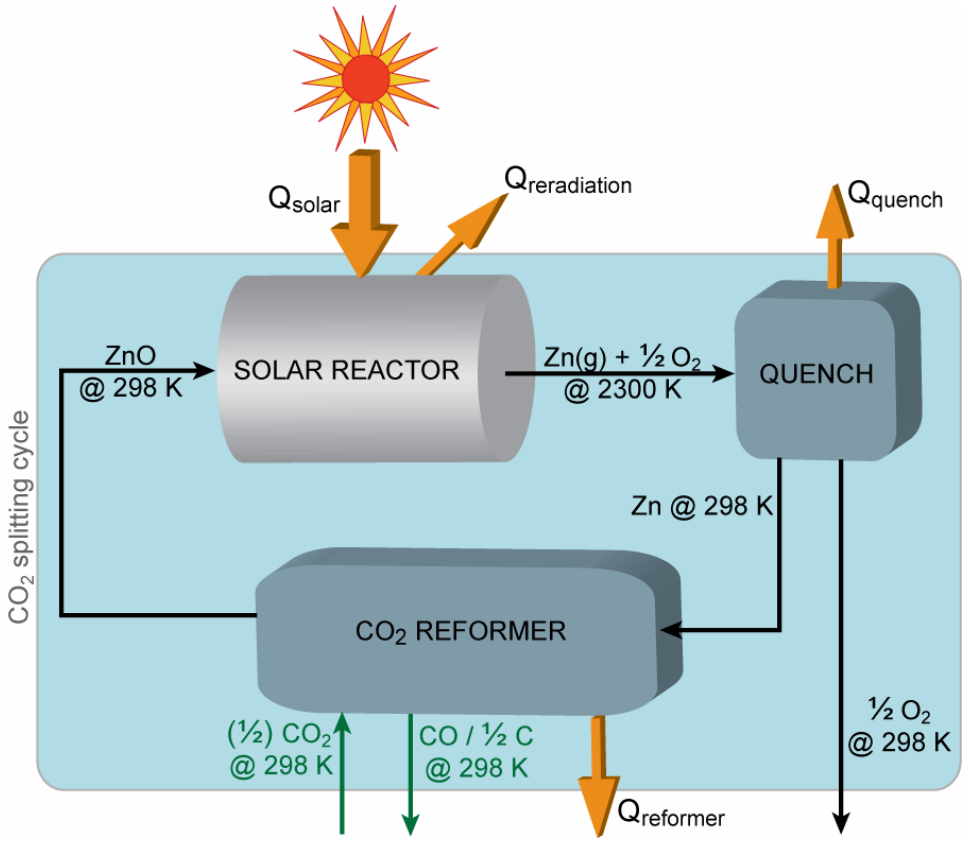


Fig. 4-1: Model flow diagram of the $CO_2$ splitting cycle comprising a solar reactor, a quench unit and a $CO_2$ reformer.

For sake of simplicity and purpose of comparison the $CO_2$ splitting cycle is based on the same ideal assumptions used by Steinfeld [20]:

- Ambient operating pressure
- Frictionless operating conditions (eliminates pressure drop and the need for pumping work)
- No heat exchangers are used for recovering sensible and latent heat
- The solar reactor behaves like a perfectly insulated blackbody cavity-receiver (no convection or conduction heat losses; effective absorptivity and emissivity approaching 1)
- Full conversion of the reactants inside the reactors

It has to be mentioned here that for the water splitting cycle chemical equilibrium inside the reactor instead of full conversion has been assumed. Since in the water splitting cycle, according to the chemical equilibrium, water is fully converted to hydrogen in the presence of zinc at ambient temperature, the different assumptions are consistent with each other. However, for the reaction of $CO_2$ with zinc it is unlikely that chemical equilibrium, i.e. full conversion to C, is reached as discussed above and verified by experimental results (see part B). Assuming chemical equilibrium inside the reactor would signify an exergy efficiency of 0 for CO at 298 K. It is therefore much more meaningful to assume full conversion of $CO_2$ to CO and C according to the proposed reactions (eq. (3.2) and eq. (3.3)).

Furthermore the following operating conditions are assumed:

- Nominal solar reactor temperature: $T_R = 2300$ K
- Normal beam insolation: $I = 1$ kW/m$^2$
- Solar concentration ratio: C = 5000, 10000
- Molar feed rate of ZnO: $\dot{n} = 1$ mol/s

### 4.1.1. Solar reactor

In the first step zinc oxide is sent to the solar reactor at ambient temperature where it is heated up to the operating temperature of 2300 K and split into zinc and oxygen. During this process the reactants absorb the net power $Q_{reactor,net}$ defined by the enthalpy change per unit time of educts and products at the corresponding temperatures:

$$Q_{reactor,net} = \dot{n}\,\Delta H\big|_{\mathrm{ZnO(s)\ at\ 298K \rightarrow Zn(g)+0.5O_2\ at\ 2300K}} \tag{4.2}$$

The solar reactor efficiency is estimated by the solar energy absorption coefficient $\eta_{absorption}$. It is defined by the net power absorbed in the solar reactor $Q_{reactor,net}$ divided by the total solar power input to the solar reactor $Q_{solar}$. It thus determines how much of the solar energy delivered to the reactor is actually stored in the Zn in terms of heat and chemical energy. For a perfectly insulated isothermal blackbody cavity-receiver the solar energy absorption coefficient is given by eq. (4.3)

where $I$ is the normal beam insulation, $T$ the nominal solar reactor temperature, $C$ the flux concentration ratio and $\sigma$ the Stefan-Boltzmann constant.

$$\eta_{absorption} = \frac{Q_{reactor,net}}{Q_{solar}} = 1 - \left( \frac{\sigma T^4}{IC} \right) \tag{4.3}$$

The corresponding irreversibilites arising from the non-reversible chemical transformation and reradiation losses to the surroundings are given by eq. (4.4).

$$Irr_{reactor} = \left( \frac{-Q_{Solar}}{2300\ \mathrm{K}} \right) + \left( \frac{Q_{reradiation}}{298\ \mathrm{K}} \right) + \left( \dot{n}\,\Delta S \big|_{\mathrm{ZnO(s)\ at\ 298K \rightarrow Zn(g)+0.5O_2\ at\ 2300K}} \right) \tag{4.4}$$

### 4.1.2. Quench unit

The products exiting from the solar reactor are Zn(g) and $O_2$(g) at 2300 K. To avoid recombination of the products they are rapidly cooled down to ambient temperature in a quench unit. The latent and sensible heat which is thereby lost to the surroundings is given by its enthalpy change per unit time:

$$Q_{quench} = -\dot{n}\,\Delta H \big|_{\mathrm{Zn(g)+0.5O_2\ at\ 2300K \rightarrow Zn(s)+0.5O_2\ at\ 298K}} \tag{4.5}$$

The irreversibility arising in the quench unit is given by:

$$Irr_{quench} = \left( \frac{Q_{Quench}}{298\ \mathrm{K}} \right) + \left( \dot{n}\,\Delta S \big|_{\mathrm{Zn(g)+0.5O_2\ at\ 2300K \rightarrow Zn(s)+0.5O_2\ at\ 298K}} \right) \tag{4.6}$$

The products of the quench unit, solid zinc and gaseous oxygen, finally are separated naturally without expending work.

### 4.1.3. $CO_2$ decomposer

In the second step the zinc is sent to the $CO_2$ decomposer where the solar energy stored as chemical energy is used to reduce $CO_2$ to CO or solid C. As the second step is exothermic, heat is released in the $CO_2$ decomposer according to eq. (4.7) and eq. (4.8) for the production of CO and C, respectively:

$$Q_{CO_2 decomposer} = -\dot{n}\,\Delta H \big|_{\mathrm{Zn+CO_2\ at\ 298K \rightarrow ZnO+CO\ at\ 298K}} \tag{4.7}$$

$$Q_{CO_2 decomposer} = -\dot{n}\,\Delta H \big|_{\mathrm{Zn+0.5CO_2\ at\ 298K \rightarrow ZnO+0.5C\ at\ 298K}} \tag{4.8}$$

In the case of CO the products again separate naturally. If the product is solid carbon, it has to be separated from the zinc oxide by an accurate separation technology. This may lead to an additional energy effort.

Because the heat released in the $CO_2$ decomposer is assumed to be lost to the surroundings, the irreversibility associated with the hydrolyser is given by eq. (4.9) when producing CO and by eq. (4.10) for the production of C, respectively.

$$Irr_{CO_2 decomposer} = \left( \frac{Q_{CO_2 decomposer}}{298\ \mathrm{K}} \right) + \left( \dot{n}\,\Delta S \big|_{\mathrm{Zn+CO_2\ at\ 298K \rightarrow ZnO+CO\ at\ 298K}} \right) \tag{4.9}$$

$$Irr_{CO_2 decomposer} = \left( \frac{Q_{CO_2 decomposer}}{298\ \mathrm{K}} \right) + \left( \dot{n}\,\Delta S \big|_{\mathrm{Zn+0.5CO_2\ at\ 298K \rightarrow ZnO+0.5C\ at\ 298K}} \right) \tag{4.10}$$

### 4.1.4. Results and Discussion

Finally, the solar-to-chemical energy conversion efficiency is calculated by using eq. (4.11) when producing CO and eq. (4.12) for the production of C.

$$\eta_{exergy} = \frac{W_{FC,ideal}}{Q_{Solar}} = \frac{-\dot{n}\,\Delta G \big|_{\mathrm{CO+0.5O_2\ at\ 298K \rightarrow CO_2\ at\ 298K}}}{Q_{Solar}} \tag{4.11}$$

$$\eta_{exergy} = \frac{W_{FC,ideal}}{Q_{Solar}} = \frac{-\dot{n}\,\Delta G \big|_{\mathrm{0.5C+0.5O_2\ at\ 298K \rightarrow 0.5CO_2\ at\ 298K}}}{Q_{Solar}} \tag{4.12}$$

Beside the work $W_{FC,ideal}$ the ideal fuel cell will also produce some heat due to the change in entropy according to eq. (4.13) and eq. (4.14) for the production of CO and C, respectively.

$$Q_{FC,ideal} = -T_L \times \dot{n}\,\Delta S \big|_{\mathrm{CO+0.5O_2\ at\ 298K \rightarrow CO_2\ at\ 298K}} \tag{4.13}$$

$$Q_{FC,ideal} = -T_L \times \dot{n}\,\Delta S \big|_{\mathrm{0.5C+0.5O_2\ at\ 298K \rightarrow 0.5CO_2\ at\ 298K}} \tag{4.14}$$

The results of the exergy analysis are given in Tab. 4-1 for two different solar concentration ratios, 5'000 and 10'000 suns. It is evident that the production of CO offers the bigger energy production potential than the production of C. Using a concentration ratio of 10'000, the exergy efficiency is 39% for CO compared to 30% for C. The Zn/ZnO cycle splitting $CO_2$ into CO shows even higher exergy efficiency than the one obtained when using the same cycle to split water into hydrogen which is 36% [20]. The reason for CO having the highest exergy efficiency is the better utilization of the energy stored in the Zn and hence generating less irreversibility in the $CO_2$ decomposer (0.21 kW/K for the production of CO compared to 0.41 kW/K for the production of C).

| | Production of CO: | | Production of C: | |
|---|---|---|---|---|
| C | 5000 | 10000 | 5000 | 10000 |
| $Q_{solar}$ [kW] | 817.17 | 663.04 | 817.17 | 663.04 |
| $Q_{reradiation}$ [kW] | 259.34 | 105.21 | 259.34 | 105.21 |
| $Q_{reactor,net}$ [kW] | 557.83 | | 557.83 | |
| $Irr_{reactor}$ [kW $K^{-1}$] | 0.81 | 0.36 | 0.81 | 0.36 |
| $Q_{quench}$ [kW] | 207.33 | | 207.33 | |
| $Irr_{quench}$ [kW $K^{-1}$] | 0.51 | | 0.51 | |
| $Q_{CO2decomposer}$ [kW] | 67.54 | | 153.75 | |
| $Irr_{CO2decomposer}$ [kW $K^{-1}$] | 0.21 | | 0.41 | |
| $Q_{FC,ideal}$ [kW] | 25.77 | | -0.43 | |
| $W_{FC,ideal}$ [kW] | 257.20 | | 197.18 | |
| $\eta_{absorption}$ | 68% | 84% | 68% | 84% |
| $\eta_{exergy}$ | 31% | 39% | 24% | 30% |

Tab. 4-1: Exergy analysis for calculating the solar-to-chemical energy conversion efficiency for the production of CO (left side) and C (right side).

Using C in an ideal fuel cell would require a heat supply from the surroundings as indicated by the negative value of $Q_{FC,ideal}$. The supplied heat is then converted to additional electrical energy which results, by definition, in a fuel cell efficiency greater than 1. This is the case due to a positive change in entropy during the reaction ($\Delta S|_{0.5C+0.5O_2 \text{ at } 298K \rightarrow 0.5CO_2 \text{ at } 298K}$ = 1.440J/K) resulting in a $\Delta G$ greater than $\Delta H$ [24].

The increase in exergy efficiency with increasing solar concentration ratio is attributed to the fact that a higher concentration factor enables to use a smaller solar receiver's aperture. Consequently re-radiation losses are minimized and the absorption efficiency is increased resulting in less irreversibility in the solar reactor. The major losses or sources of irreversibility are associated with the re-radiation losses from the solar reactor and the quenching of products. E.g. for a concentration factor of 5000 suns, re-radiation accounts for 32% loss of the input solar power and quenching for 25% loss. As already mentioned, re-radiation losses could be minimized by increasing the solar concentration ratio. The loss resulting from quenching the products could be minimized by recovering the heat, e.g. by heat exchangers. However heat recovering is limited because efficient quenching requires a high quench rate in order to avoid recombination of the products. But a high quench rate is unfavourable for heat recovering.

## 4.2. Solar-to-electricity energy conversion efficiency

### 4.2.1. Power generation units

A more realistic efficiency is obtained by calculating the solar-to-electricity energy conversion efficiency taking into account the losses occurring in reality when converting chemical energy into electricity. For this reason three suitable power generation units have been added to the $CO_2$-splitting cycle (Fig. 4-2).

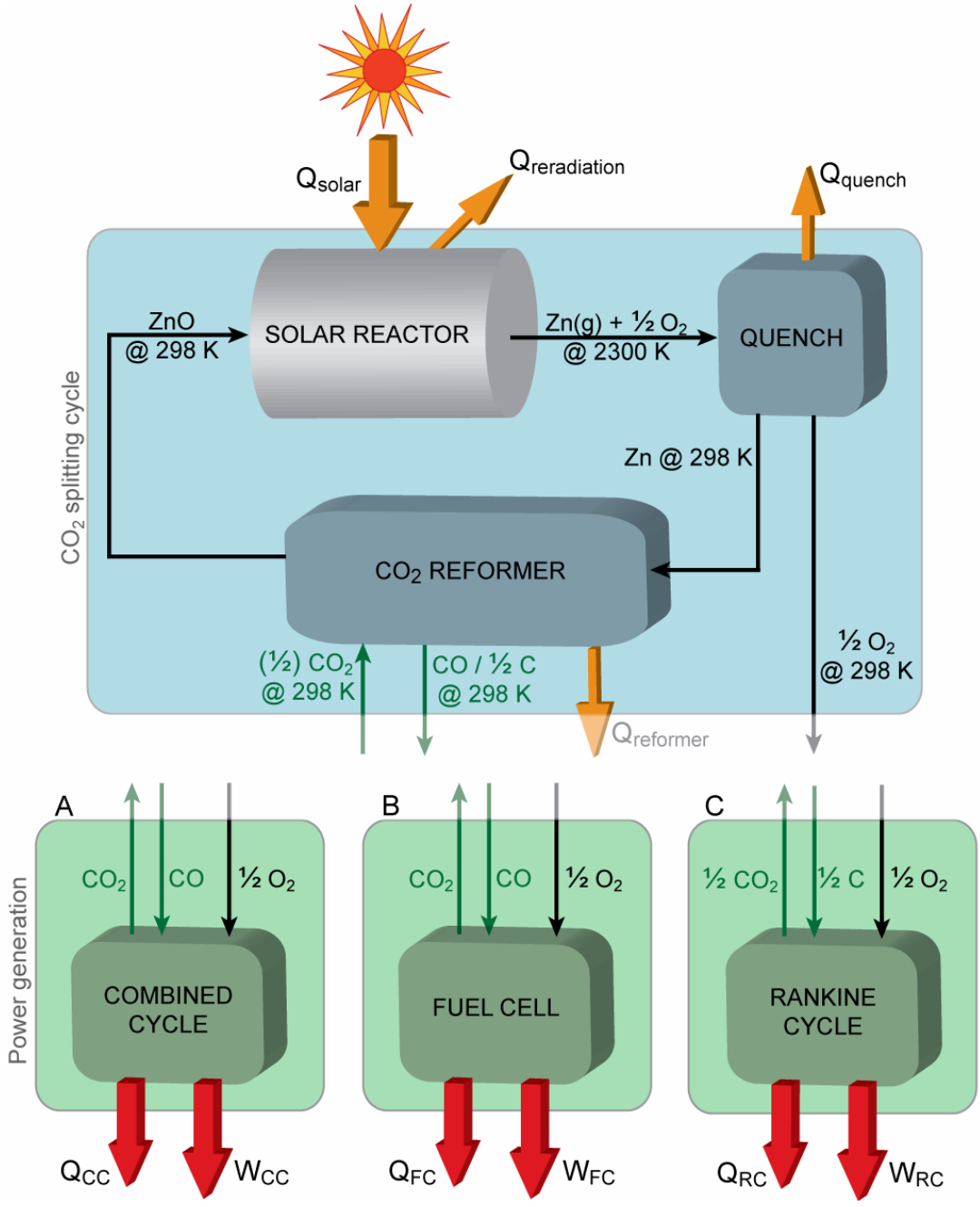


Fig. 4-2: Model flow diagram of the 2-step $CO_2$ splitting cycle in combination with 3 possible power generation units for the production of electricity and heat.

A CO is used in a combined cycle with an efficiency of 60% (fuel to electricity) producing heat $Q_{CC}$ and electricity $W_{CC}$ according to eq. (4.15) and eq. (4.16).

$$W_{CC} = -\eta_{CC}\dot{n}\,\Delta H\big|_{\mathrm{CO+0.5O_2\ at\ 298K \rightarrow CO_2\ at\ 298K}} \tag{4.15}$$

$$Q_{CC} = -(1-\eta_{CC})\times\dot{n}\,\Delta H\big|_{\mathrm{CO+0.5O_2\ at\ 298K \rightarrow CO_2\ at\ 298K}} \tag{4.16}$$

B CO is used in a high-temperature fuel cell with an efficiency of 60% (fuel to electricity) producing heat $Q_{FC}$ and electricity $W_{FC}$ according to eq. (4.17) and eq. (4.18).

$$W_{FC} = -\eta_{FC}\dot{n}\,\Delta G\big|_{\mathrm{CO+0.5O_2\ at\ 298K \rightarrow CO_2\ at\ 298K}} \tag{4.17}$$

$$\begin{aligned} Q_{FC} = &-T_L\times\dot{n}\,\Delta S\big|_{\mathrm{CO+0.5O_2\ at\ 298K \rightarrow CO_2\ at\ 298K}} \\ &-(1-\eta_{FC})\times\dot{n}\,\Delta G\big|_{\mathrm{CO+0.5O_2\ at\ 298K \rightarrow CO_2\ at\ 298K}} \end{aligned} \tag{4.18}$$

C Solid carbon is used in a Rankine Cycle with an efficiency of 35% (fuel to electricity) producing heat $Q_{RC}$ and electricity $W_{RC}$ according to eq. (4.19) and eq. (4.20).

$$W_{RC} = -\eta_{RC}\dot{n}\,\Delta H\big|_{\mathrm{0.5C+0.5O_2\ at\ 298K \rightarrow 0.5CO_2\ at\ 298K}} \tag{4.19}$$

$$Q_{RC} = -(1-\eta_{RC})\times\dot{n}\,\Delta H\big|_{\mathrm{0.5C+0.5O_2\ at\ 298K \rightarrow 0.5CO_2\ at\ 298K}} \tag{4.20}$$

### 4.2.2. Results and Discussion

The exergy efficiency is then expressed by the work (electricity) output of the corresponding power generation unit divided by the solar input:

$$\eta_{exergy} = \frac{W_{CC/FC/RC}}{Q_{Solar}} \tag{4.21}$$

The results are given in Tab. 4-2 for a solar concentration ratio of 10'000 suns and a molar feed rate of 1 mol/s ZnO. The highest exergy efficiency for electricity production is 26% and obtained by producing CO and using it in a combined cycle. When using CO in a fuel cell, the exergy efficiency is somewhat lower at 23% although both power generation units are considered to work with efficiency (fuel to electricity) of 60%. The difference in the final exergy efficiency is due to different definitions of the electricity output (eq. (4.15) and eq. (4.17)). A fuel cell converts chemical into electrical energy and the electricity output is hence given by the change in Gibbs energy. However, for the combined cycle, which transforms heat into electricity, the electricity output is given by the total heat input which is equal to the change in enthalpy and thus including heat production due to an increase in entropy. Regarding the exergy efficiency a positive change in

entropy as it is the case for the combustion of CO with oxygen leads therefore to an advantage of the combined cycle over the fuel cell.

| | Combined Cycle | Fuel Cell | Rankine Cycle |
|---|---|---|---|
| $Q_{solar}$ [kW] | 663.04 | 663.04 | 663.04 |
| $\eta_{power\ generation}$ | 0.6 | 0.6 | 0.35 |
| $W_{electricity}$ [kW] | 169.78 | 154.32 | 68.86 |
| $Q_{heat}$ [kW] | 113.18 | 128.65 | 127.89 |
| $\eta_{exergy}$ | 26% | 23% | 10% |

Tab. 4-2: Results of the exergy analysis estimating the solar-to-electricity conversion efficiency of the $CO_2$-splitting cycle in combination with three different power generation units.

Fuel cells able to use CO as a fuel are high-temperature fuel cells such as the molten carbonate fuel cell (MCFC) or the solid oxide fuel cell (SOFC). For both types fuel-to-electricity efficiencies of 50-60% are reported [25]. If pure CO is used in a combined cycle, further investigations concerning combustion characteristics in the gas turbine are required. A change in fuel will change basic combustion aspects such as flame speed or temperature. In context with a recently suggested "$CO_2$ decomposition-based power generation cycle" the influence of adding CO to the conventional fuel, methane, was studied [26]. Thereby it has been reported, that increasing CO fraction in the fuel improves the flame stability characteristics.

CO is a toxic gas restricting transport and handling. It should therefore be produced and used on-site either by the suggested power generation units or further processed to liquid fuels, e.g. methanol [27]. By using carbon as a fuel, transport and handling gets much easier. The drawback however will be, that C used in a Rankine cycle offers an exergy efficiency of only 10%. When aiming at the production of electrical power, CO should be preferred to C. The issue of transport can be solved by separating the solar reactor and the $CO_2$ reformer. At a solar rich place, ZnO is reduced to Zn in the solar reactor. The Zn can then be transported to an existing fossil fuel power plant, where the $CO_2$ emissions are captured and fully or partly reduced to CO. The CO may then be reused within the existing infrastructure as a fuel and hence will substitute further energy input from fossil fuels. Finally the ZnO is transported back to the solar reactor, where it will be recycled again to Zn.

# 5 Economic analysis - carbon sequestration

The $CO_2$-splitting cycle can be thought of as an open cycle, splitting $CO_2$ into solid carbon and oxygen (Fig. 5-1). The solid carbon may then be used as a stable and safe sequestration product either in the ground or in chemical industry.

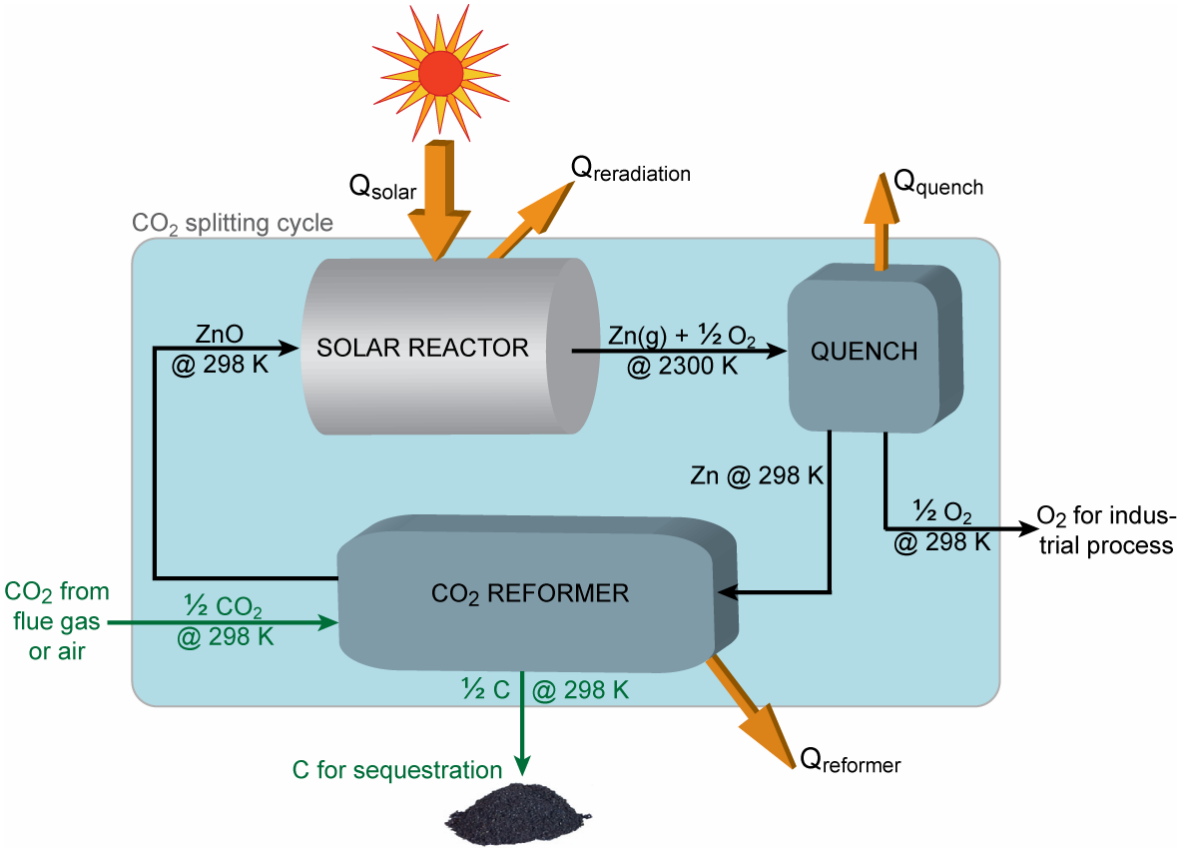


Fig. 5-1: Model flow diagram of the 2-step $CO_2$ splitting cycle for the production of solid carbon.

The overall costs for the production of carbon via the suggested cycle have been calculated by an economic analysis based on the assumptions of Steinfeld [20]. For the solar concentrating plant a solar tower system with a Cassegrain optical configuration which delivers 90 $MW_{th}$ of concentrated solar power to the solar reactor was assumed [28]. An annual beam irradiation of 2300 $kWh_{th}/m^2/yr$ and 2300 equivalent full power hours were taken as baseline parameters. In order to deliver the requested 90 $MW_{th}$, a Heliostat area of 155'172 $m^2$ will be needed. Efficiencies and costs for the various steps are taken from [20] where the same Zn/ZnO cycle was used to calculate the costs of solar hydrogen production. The only difference to the $CO_2$ splitting cycle is the use of the $CO_2$ reformer instead of a Hydrolyser. Because they both aim at the same chemical process, namely the oxidation of zinc in presence of a reactant gas which will be reduced thereby, they are assumed to be equal in terms of cost. The results of the cost analysis are given in Tab. 5-1 for two different solar concentration ratios: 5'000 and 10'000.

| Solar concentration ratio [-] | 5000 | 10000 |
|---|---|---|
| Optical efficiency, $\eta_{optics}$ | 58% | 58% |
| Solar reactor's absorption efficiency, $\eta_{absorption}$ | 68% | 84% |
| $Q_{reactor,net}$ [MW] | 61.2 | 75.6 |
| ZnO feed [t/h] | 32.2 | 39.7 |
| Zn production [t/yr] | 59'419 | 73340 |
| $CO_2$ consumption [t/yr] | 19'985 | 24'687 |
| C production [t/yr] | 5'450 | 6'733 |
| | | |
| Capital cost for solar C [M$] | 55.08 | 60.38 |
| Annual fixed charge rate | 15% | 15% |
| Annual capital cost for solar C [M$/yr] | 8.26 | 9.06 |
| O&M cost for solar C [M$/yr] | 1.10 | 1.21 |
| Total annual cost for solar C [M$/yr] | 9.36 | 10.26 |
| | | |
| Unit cost of solar C [$/t] | 1'717.7 | 1'524.9 |
| Unit cost of solar $CO_2$ mitigation [$/t] | 468.5 | 415.9 |

Tab. 5-1: Estimated costs of solar C production and solar $CO_2$ mitigation.

For a solar concentration between 5000 and 10'000 suns, the economic evaluation predicts a unit cost of 1525-1718 $/tC produced or a unit cost of 416-469 $/t$CO_2$ avoided i.e. converted to stable and harmless C. This is rather high compared to geological storage where costs of 0.6 – 8.3 $/ton$CO_2$ (including monitoring and verification) are predicted [29]. However geological storage offers severe disadvantages concerning safety and long-term stability due to leakage. For a proper comparison, the risk of negative environmental impact, e.g. due to leakage should be monetarized and added to the cost for geological storage. A much more stable method for $CO_2$ sequestration is mineral carbonation. Similar to the proposed $CO_2$ splitting cycle, the $CO_2$ is converted by chemical reactions to a solid, in this case to inorganic carbonates. For mineral carbonation the estimated costs are 50-100$/t $CO_2$ net mineralized. However one ton of $CO_2$ stored as carbonate produces 2.6 to 4.7 tonnes of material to be disposed. This would therefore be a large operation with an environmental impact similar to that of current large-scale surface mining operations [29]. The proposed $CO_2$ splitting cycle offers here a big advantage: for mitigating one ton of $CO_2$ it produces only ~0.3 tonnes of disposable material, i.e. carbon. This will reduce material transport/storage and the corresponding environmental impact by a factor 10 compared to mineral carbonation.

# B. Experimental Analysis

# 6 Oxidation of zinc - review

In 1973, Lawless presented a detailed review of the principles governing oxidation of metals [30]. He divided the different stages of metal oxidation into:

(1) The initial stages of oxidation
(2) Oxide film formation
(3) Thick film and scale formation

Assuming that initially a true clean metal surface is available, (1) involves adsorption (chemisorption) onto the metal followed by incorporation of the oxygen into the metal. This leads to an undefined layer of oxygen interacting with the metal surface (induction period). Through nucleation processes, possibly due to supersaturation of the superficial region of the metal with oxygen, oxide nuclei are formed on the metal surface signalling the end of the induction period. These nuclei are apparently randomly distributed over the metal surface and grow rapidly in lateral directions until the surface is covered. Although the growth mechanism is not clear, the nuclei may grow by surface diffusion of the adsorbed oxygen to a nucleus leaving an oxygen depletion zone about each nucleus where no other nuclei may form (Fig. 6-1).

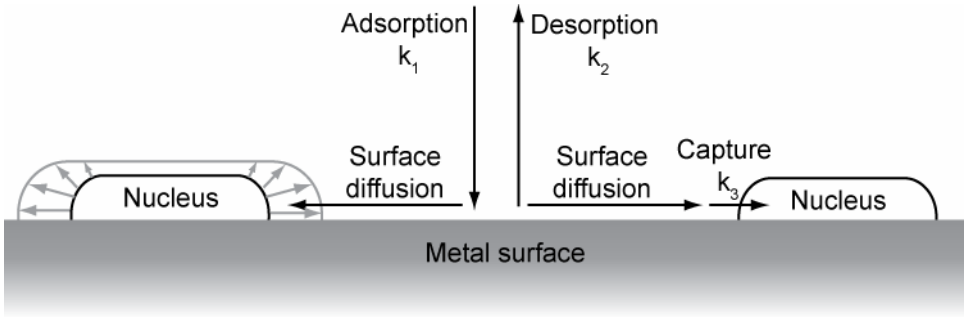


Fig. 6-1: Model for growth of oxide nuclei on metal surface (based on Lawless). $k_1$, $k_2$ and $k_3$ are the rate constants for adsorption, desorption and capture of adsorbed oxygen by the oxide island.

Once a continuous film of oxide has formed on the metal surface, the metal and gaseous reactants are spatially separated by a barrier. For the formation of thin films (< 600 nm) (2) a number of theories have been proposed, based on different rate-limiting processes such as:

- anion or cation diffusion through the bulk oxide
- mass or charge transport across one of the interfaces
- electron transfer processes associated with the chemisorption of oxygen

These theories lead to inverse or direct logarithmic, parabolic, cubic, quartic or linear rate laws mostly applicable at low and intermediate temperatures. It is thereby pointed out that diffusion

along grain boundaries and dislocations may play an important role since it is considerably greater than lattice diffusion via point defects.

For thick film and scale formation (3), i.e. oxide films greater than 600 nm, the growth law most commonly observed is parabolic. Usually such oxide films are formed at elevated temperatures and the mechanism of oxidation primarily depends on the detailed nature of the oxide formed. Point defects (vacancies, interstitials), line defects (dislocations) and planar defects (stacking faults, grain-boundaries) are responsible for material transport within the oxide and may play a critical role. Based on the ambipolar diffusion of reactants via point defects the best known theory of parabolic growth is the Wagner theory. Thereby it is assumed, that phase boundary reactions are rapid with respect to the rate-determining diffusion processes. The requirements for the verification of Wagner's theory are a dense, homogenous and relatively thick layer of oxide [31]. In the case of an oxide layer containing pores or cracks, mass transport across the oxide layer may be facilitated and enhance the oxidation rate. Phase boundary reactions may then become the rate-limiting step, leading to linear oxidation kinetics.

Summarized, it is obvious, that oxidation of metals is strongly dependent on the microstructural features and the thickness of the formed oxide layer. When comparing different experimental results from literature it is therefore important to distinguish carefully between the conditions such as particle size, temperature range and gas pressure/composition under which the experiments were carried out.

One of the first comprehensive studies about zinc oxidation was performed by Vernon et al. in 1939 [32]. They investigated the oxidation of zinc plates with air at atmospheric pressure using temperatures ranging from 298 to 673 K. The relationship between oxidation and time was described by a direct logarithmic equation over the whole temperature range:

$$W = k \cdot \log(at + 1) \tag{6.1}$$

$W$ is the amount of oxidation in mg/dm$^2$, $k$ and $a$ are temperature-dependent parameters. Below a critical temperature of 498 K, they observed an extremely low oxidation depending remarkably upon surface condition. Above this temperature a great increase in the oxidation rate has been observed. This behaviour was explained by an initial formation of an amorphous oxide film being continuous, compact, and relatively impervious to diffusion of both oxygen and zinc. The enhanced oxidation rate above the critical temperature was attributed to facilitated diffusion due to crystallization of the amorphous layer. Furthermore, in some experiments, they observed a stable surface oxide film isolated by volatilization of the underlying zinc at comparatively low temperatures (673 K).

Some years later, in 1950, Moore and Lee [33] studied the oxidation kinetics of zinc foils with oxygen in the temperature range of 573-673 K at low pressures (< 0.53 bar). The oxidation rates were measured by following the volumetric uptake of oxygen at constant temperature and pressure. The oxidation rates were then expressed in terms of oxide film thickness leading to a thickness

range of 20-100 nm. In agreement with Vernon et al., at lower temperatures, < 623 K, the rate followed a logarithmic equation. But above 643 K, the rate followed a parabolic equation, eq. (6.2), where y is the growing oxide-film thickness and k the parabolic rate constant.

$$\frac{dy}{dt} = \frac{k}{y} \tag{6.2}$$

The logarithmic rate law at lower temperatures has been explained on the basis of Vernon et al. that the zinc surface first becomes covered at certain spots or patches. These then grow laterally until the entire surface is covered and further oxidation is virtually stopped. The parabolic rate law at higher temperatures (643-673 K) was explained by a model based on the Wagner theory including the following steps (Fig. 6-2):

1. Activated adsorption of $O_2$ as O atoms on the surface of ZnO
2. Conversion of adsorbed O atoms into adsorbed $O^{2-}$ ions by electrons that pass from the underlying metal to the oxide-oxygen interface
3. $Zn^{2+}$ ions migrating from the metal through the oxide

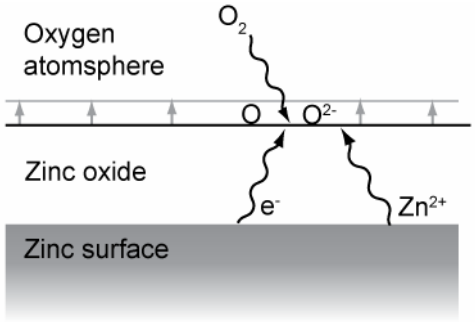


Fig. 6-2: Rough model of the processes occurring in oxidation of zinc according to Moore and Lee [33].

Due to the marked dependence of pressure below 0.13 bar, the rate-determining step of the reaction is believed to be the activated adsorption of oxygen leading to an activation energy of 295.2 kJ/mol. At higher oxygen pressure, the oxidation reaction was diffusion-controlled and a lower activation energy of 119.3 kJ/mol was calculated.

Similar results have been obtained by Tuck, Whitehead and Smallman [34] who investigated the oxidation of zinc plates at 593-688 K in oxygen by gravimetry. Thickness of the oxide layer ranged up to 1 µm. At ambient pressure and below 643 K, zinc oxidation obeys logarithmic kinetics yielding an activation energy of 209 kJ/mol. Above 648 K the oxidation follows a parabolic law resulting in a lower activation energy of 92 kJ/mol. Due to a strong dependence on oxygen partial pressure in the range of $p_{O_2} = 0.001 - 1$ bar, a reaction mechanism involving control of oxidation at the oxide/oxygen interface has been proposed. For the logarithmic kinetics the rate controlling step

is believed to be the reaction $O^- + e^- \rightarrow O^{2-}$, whereas for the parabolic kinetics at higher temperatures it is believed to be the incorporation of oxygen ions.

Several newer studies investigating the oxidation of zinc have been carried out with zinc micro- and nanoparticles. Ernst [35] performed thermogravimetric analysis of the hydrolysis of submicron zinc particles (mean particle size = 163 nm) in the temperature range of 603-633 K. He observed an initial fast surface reaction with a linear conversion profile, proceeding with half-order dependence on water vapor (y). This suggested that the initial oxidation rate is reaction-limited such as by dissociation of the water molecules on the Zn/ZnO surface, leading to an activation energy of 42.8 kJ/mol. However, this fast early kinetics was only valid for a weight increase up to 2 % (~8% conversion, reaction time < 1 min). The subsequent slower hydrolysis was independent of y and following a parabolic law. The observed reactivity was explained by a core-shell model based on the Wagner-theory, consisting of a Zn core and a ZnO shell superstoichiometric in terms of Zn leading to the formation of interstitial $Zn^{2+}$ ions. In contact with the reaction gas, the surface ions react to ZnO and deplete the surface from Zn resulting in zinc ion concentration. The reaction limiting step is hence the diffusion of the interstitial $Zn^{2+}$ from the core through the shell resulting in an activation energy of 42.9 kJ/mol. This comparatively low activation energy was explained by a facilitated dissolution of Zn from the core into the shell when using small zinc particles.

Nakamura et al. [36] studied the oxidation of freshly produced zinc nanoparticles at 383 and 423 K. Similar to Ernst they observed a steep drop off in the oxidation rate after the formation of an initial zinc oxide layer. Based on the low-temperature theory they believe that in a thin oxide layer the diffusion of Zn ions is enhanced due to the establishment of an electronic field across the layer. Above a critical oxide thickness, thermally activated ion migration is necessary for further growth. At a temperature of 423 K this critical thickness was found to be 10nm and no further growth was observed due to the low mobility of the Zn ions in the ZnO at 423 K. As a consequence, only particles with diameters less than 20 nm were completely oxidised and formed hollow ZnO particles.

The formation of hollow ZnO cages and shells has also been observed by Gao and Wang [37]. Sublimated Zn atoms were carried from a high termperature regime to a lower one at 573-773 K. This led to the formation of Zn polyhedra due to condensation and solidification of the Zn atoms. The surface of the Zn polyhedra then was subsequently oxidised by residual oxygen left in the growth chamber. Due to a large lattice mismatch of Zn and ZnO (23.7 %), the oxidation takes place in terms of ZnO nanocrystallites forming multinuclei on the Zn surface. By further growth of these nuclei a mesoporous ZnO structure is formed. An increase in local temperature during the growth may then lead to sublimation of Zn resulting in the formation of textured ZnO shell/cage structures. A similar mechanism was also reported by Sulieman et al. [38]. Above 673 K they found partly opened ZnO/Zn microspheres having a hollow interior with a diameter of 4-6 µm and a shell thickness of about 1 µm. Below 673 K they found Zn/ZnO microspheres mainly consisting of Zn. It is believed that above 673 K, Zn atoms are vaporized and escape from the centre of the ZnO/Zn microspheres by breaking the shell of the spherical ZnO structure, resulting in the formation of a hollow-opened ZnO/Zn spherical structure.

An intensive examination of the literature has shown that for the oxidation of zinc there is no explicit oxidation law. Oxide thickness and structure covering the zinc seem to have a main influence on the reaction rate. The structure of the oxide layer again is dependent on a bunch of parameters: oxidizing gas composition and partial pressures, temperature and initial zinc surface (e.g. impurities). It is, therefore, nearly impossible to explain advanced zinc oxidation using a single model because the boundary conditions are continuously changing with progressing oxidation. A more phenomenological approach is adopted here in order to obtain some reasonable ideas for a further reaction study.

In the following list some general observations taken from literature are summarized:

- Assuming an initial clean zinc surface a fast initial oxidation is expected.
- The growing oxide layer limits oxidation rate drastically and diffusion processes become important.
- Thickness and structure of the oxide layer influences strongly the diffusion through the layer.
- Higher temperature enhances diffusion and leads to thicker oxide layers.
- At lower temperature ( < 673K) $Zn^{2+}$ ions may become the limiting diffusion species.
- The exothermic reaction may lead to local temperature increase and change diffusion processes.
- At higher temperatures ( > 673 K) zinc sublimation starts and enhances diffusion through formation of cracks in the outer ZnO shell.
- Higher initial partial pressure of oxidant increases number of nuclei leading to more grain boundaries which may enhance ion diffusion processes at lower temperatures.
- Lower initial partial pressure of oxidant leads to few nuclei enhancing shear stresses and provoking cracks which may facilitate diffusion of sublimated zinc at higher temperatures.

# 7 Kinetic Study

## 7.1. Setup

The oxidation of zinc has been studied in a thermogravimeter system (TG, Netzsch STA 409 CD) with a high temperature furnace equipped with a spiral SiC-heating tube suitable for temperatures up to 1823 K. The change in sample mass is determined by an analytical balance system, which is located in a vacuum tight casing and connected to the furnace with a cross head. A sample carrier system containing a radiation shield and an S-type thermocouple (Pt10%/Pt-Rh) is plugged to the balance system. The samples were placed in an $Al_2O_3$ pan (TG sample carrier) on top of the sample carrier system. An evacuating system (two-stage rotary pump) is attached to the rear of the balance casing. For protection and to prevent influences on the weight measurement, the balance system was continuously purged with a constant argon flow of at least 10ml/min. The reducing gas, $CO_2$ or CO in combination with Ar, is introduced at the bottom of the sample chamber through the cross head valve. It is then directed upwards together with the purge gas from the balance system to the sample carrier. The exhaust gas, exiting on top of the sample chamber, was then cooled down and filtrated by a sample gas conditioner (AGT MAK 10) and subsequently analysed by gas chromatography (two-channel Varian Micro GC, equipped with Molsieve-5A and Poraplot-U columns). The gas flow rates were adjusted by a manual mass flow controller (Netzsch gas control). The temperature profile was programmed and controlled by a system controller (Netzsch TASC 414/4) and recorded on a PC with the corresponding software (Proteus 4.1).

## 7.2. Parameters

The experimental campaign with the TG was carried out within the following set of parameters:

- Sample: Zinc, Dust (Sigma-Aldrich, < 10 µm, 98+ %)
- Mean particle size: ~10 µm (measured by Particle Size Distribution Analyser, Horiba LA 950)
- Temperature, iso. runs: 623 – 823 K
- Temperature dyn. runs: up to 1153 K (heating range 5-25 K/min)
- Reactant gas: $CO_2$ (Pangas 4.5, ≥ 99.995%) or CO (Messer 4.7, ≥ 99.997%)
- Carrier gas: Ar (Messer Schweissargon, ≥ 99.996%)
- Total gas flow: 0.1-0.2 l/min
- $CO_2$ partial pressure: 4.6 – 1000 mbar (corresponds to $CO_2$ concentration of ~0.5 – 100%)

## 7.3. Procedure

A sample of approximately 100 mg pure Zn dust was put on the $Al_2O_3$-crucible. The crucible was then placed on top of the sample carrier system of the TG. The oxygen content in the balance casing

and sample chamber was reduced to a minimum by evacuating it three times and filling it with argon. With the GC it was ensured, that oxygen concentration in the TG was below 40 ppm. For the isothermal runs, the reaction zone was heated up to the desired isothermal temperature under Ar flow. After the temperature stabilized the desired amount of reactant gas ($CO_2$ or CO) was introduced. Simultaneously the Ar flow was reduced in such a way, that the overall gas flow was kept constant avoiding any influence on the balance. Temperature and gas flow then were kept constant until the end of the reaction, i.e. when no further mass change was registered by the TG. For the dynamic runs, the samples were heated up in the reactant gas using a constant heating range. The produced gases were analyzed with the GC and the change of mass was recorded with the corresponding software connected to the TG. When reaching the end of the experiment, the samples were cooled down in Argon. The products were then characterized by x-ray powder diffraction (XRD, Philips XPert-MPD powder difractometer) and $N_2$ –adsorption (BET, Micromeritics 3000). Furthermore pictures of selected samples have been taken by scanning election microscopy (SmartSEM, Carl Zeiss Supra 55VP).

## 7.4. Observations

Fig. 7-1 shows weight gain, temperature profile and gas concentrations in the outlet gas of a typical isothermal TG run (isothermal temperature: 673 K, $CO_2$ partial pressure: 6.2 mbar).

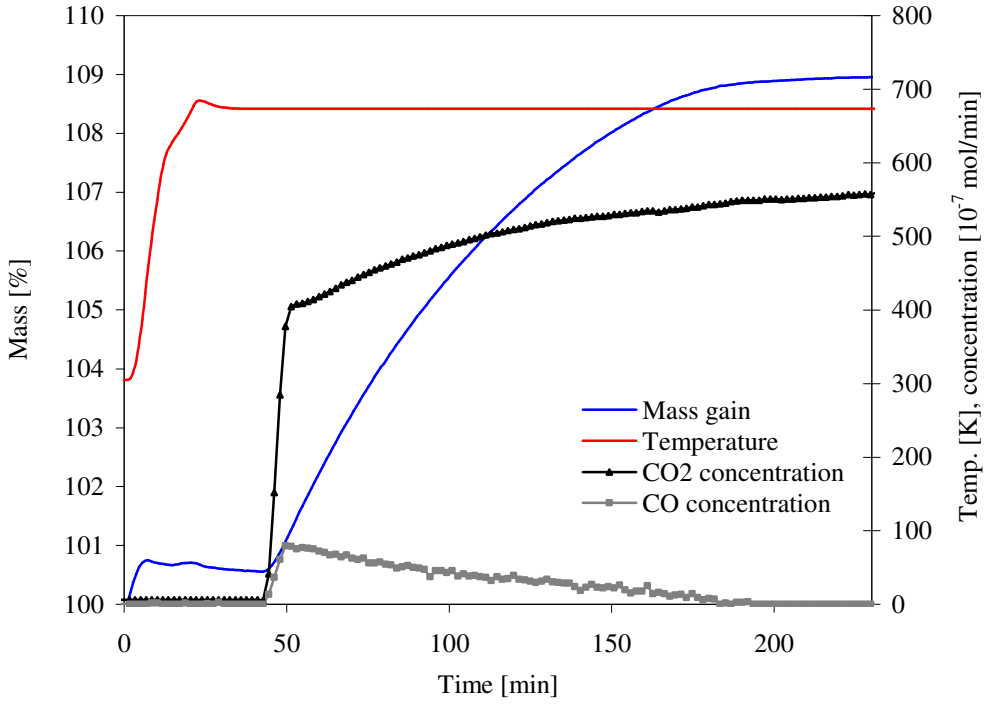


Fig. 7-1: Mass gain, temperature profile and gas concentrations in the outlet gas as a function of time during the isothermal TG run of Zn oxidation with $CO_2$ (6.2 mbar partial pressure) in Argon at 673 K and 1 bar.

In the initial stage of heating up a slight mass increase of ~0.8% is observed due to buoyancy effects. However, above 500 K the mass always stabilized. After having reached the isothermal temperature of 673 K, the $CO_2$ was injected (t = ~45 min). The immediate increase of the mass due to the conversion of Zn into the heavier ZnO and the formation of CO indicate that the reaction takes place according to eq. (3.2). From the point of $CO_2$ injection it takes ~6 min until the $CO_2$ concentration stabilizes on the set level. This delay arises as a consequence that the gas flows are quite small compared to the volumes (tubes and sample chamber). The $CO_2$ concentration then gradually increases towards the end of the reaction and to the set level as less $CO_2$ is consumed. The change in mass is characterized by a steep initial increase which then flattens down until mass increase approaches a stable level signalling the end of the reaction. An even steeper increase is observed for the CO evolution followed by a drop in concentration towards the end.

An example of a typical dynamic TG run is given in Fig. 7-2 for a $CO_2$ partial pressure of 638 mbar. The sample chamber was heated up in $CO_2$ with a heating range of 10 K/min up to a temperature of 1073 K.

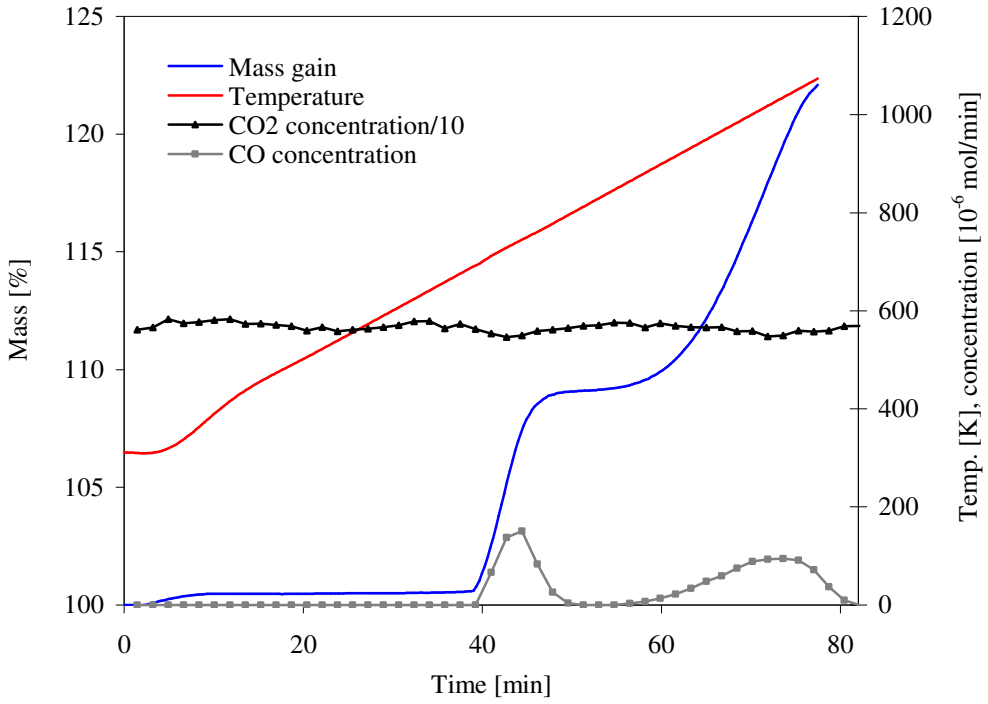


Fig. 7-2: Mass gain, temperature profile and gas concentrations in the outlet gas as a function of time during the dynamic TG run of Zn oxidation with $CO_2$ (638 mbar partial pressure) in Argon at 1 bar.

During reaction no clear change in $CO_2$ can be observed as the amount of $CO_2$ consumed is too small compared to the set concentration. However the mass change and the CO formation clearly indicate the desired proceeding of the reaction. The mass increase starts at around 690 K and proceeds almost linear until it levels down at 800 K. When heating further up, the reaction is accelerated again at around 860 K and progressing linearly until reaching almost full conversion,

21.6% mass increase from the start of reaction, where the experiment was stopped. Full conversion would correspond to a mass increase of 24.5 %. The XRD measurement of the product revealed a molar percentage of 97.1% ZnO, which is slightly higher than the conversion according to the mass increase in the TG. The slight difference could occur from measurement uncertainty, e.g. due to the automatic stop of the mass change recording when having reached the final temperature even though the reaction was still going on for a while as can be concluded from the CO formation. Another possible explanation could be a small loss of zinc sample due to vaporization as it has been observed when heating up the sample in argon. In an inert atmosphere, without $CO_2$, considerable zinc evaporation has been observed above 673 K. At 823 K an evaporation rate of $5.80 \cdot 10^{-5}$ mol/min zinc was measured (see Fig. 7-3). This would be enough to let the entire sample evaporate within 26 min! However, the results obtained in the dynamic run revealed, that in the presence of a small amount of $CO_2$ almost all zinc is converted to ZnO without leaving the crucible, even when heating up to high temperatures (1073 K).

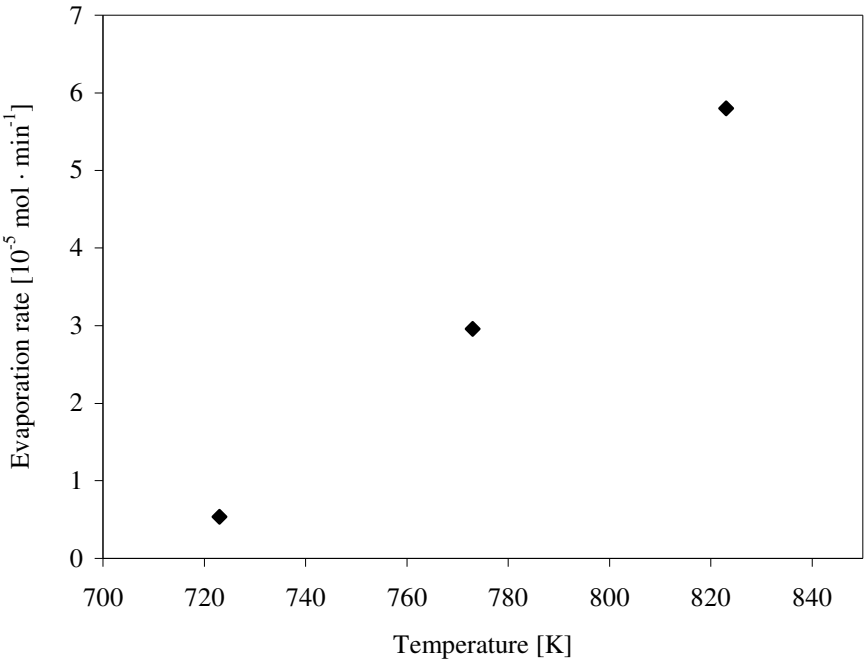


Fig. 7-3: Evaporation rate of zinc in argon at 1 bar as a function of temperature, measured in the TG

## 7.5. Data Acquisition

For each experiment the reaction extent was calculated based on the Zn to ZnO conversion measured by the weight increase in the TG. According to reaction 2a and 2b for each mole of ZnO produced, one mole of Zn is consumed. The Zn conversion is hence given by the number of moles ZnO at time t, $n_{ZnO}^{t}$, divided by the initial number of moles Zn placed in the TG-crucible, $n_{Zn}^{0}$ (eq.(7.1)).

$$X_{Zn} = \frac{n_{ZnO}^{t}}{n_{Zn}^{0}} \tag{7.1}$$

$n_{Zn}^{0}$ and $n_{ZnO}^{t}$ are calculated using eq. (7.2) and eq. (7.3) with $M_{Zn}^{0}$ the initial mass of Zn, $\tilde{M}_{Zn}$ and $\tilde{M}_{ZnO}$ the molar mass of Zn and ZnO, respectively, and $Wt\%$ the percentage mass gain measured by the TG.

$$n_{Zn}^{0} = \frac{M_{Zn}^{0}}{\tilde{M}_{Zn}} \tag{7.2}$$

$$n_{ZnO}^{t} = \frac{Wt\% \cdot M_{Zn}^{0}}{\tilde{M}_{ZnO} - \tilde{M}_{Zn}} \tag{7.3}$$

Eq. (7.3) assumes no loss of any species during reaction and no production of C. In the case of C production, $n_{ZnO}^{t}$ would be given by eq. (7.4) including $M_{C}^{t}$, the mass of C produced at time t.

$$n_{ZnO}^{t} = \frac{Wt\% \cdot M_{Zn}^{0} - M_{C}^{t}}{\tilde{M}_{ZnO} - \tilde{M}_{Zn}} \tag{7.4}$$

Alternatively the reaction extent is calculated by the CO yield, $Y_{CO}$, and the C yield, $Y_{C}$, given by eq. (7.5) and eq. (7.6), respectively.

$$Y_{CO} = \frac{n_{CO}^{t}}{n_{Zn}^{0}} \tag{7.5}$$

$$Y_{C} = \frac{2 \cdot n_{C}^{t}}{n_{Zn}^{t}} \tag{7.6}$$

$n_{CO}^{t}$ and $n_{C}^{t}$ are the accumulated numbers of moles of CO and C at time t. While CO is directly measured by the GC this is not possible for C. However, the number of moles C can be calculated indirectly by applying a “C-balance”, given by eq. (7.7).

$$n_{C}^{t} = n_{CO_2,consum}^{t} - n_{CO}^{t} \tag{7.7}$$

$n_{CO_2,consum}^{t}$ corresponds to the accumulated number of moles $CO_2$ consumed at time t which is measured by the GC. It was calculated by subtracting the number of moles $CO_2$ measured by the GC at time t from a baseline which was taken at the end of the reaction, when no $CO_2$ was consumed anymore.

Based on the $CO_2$ consumption the reaction extent may also be expressed by applying eq. (7.8).

$$X_{CO_2} = \frac{n^t_{CO_2,consum}}{n^0_{Zn}} \tag{7.8}$$

Finally, the reaction extents can be verified using eq. (7.9).

$$X_{Zn} = Y_{CO} + Y_C = X_{CO_2} \tag{7.9}$$

Fig. 7-4 shows exemplary the three different reaction extents for the isothermal run at 673 K and with a $CO_2$ partial pressure of 6.2 mbar. The curves show quite good results for experiments using low $CO_2$ concentration. For high concentrations however, the correlation reduces because it is not possible to extract a baseline for the calculation of $n^t_{CO_2,consum}$ anymore (compare with Fig. 7-2). Furthermore, the CO yield strongly depends on the GC measurement which is less reliable than the mass measurement of the TG due to high variations in the concentrations. Therefore, for further discussions, only the conversion calculated from the TG results, $X_{Zn}$, are used. The CO yield thereby serves as an instrument to judge a possible production of solid C.

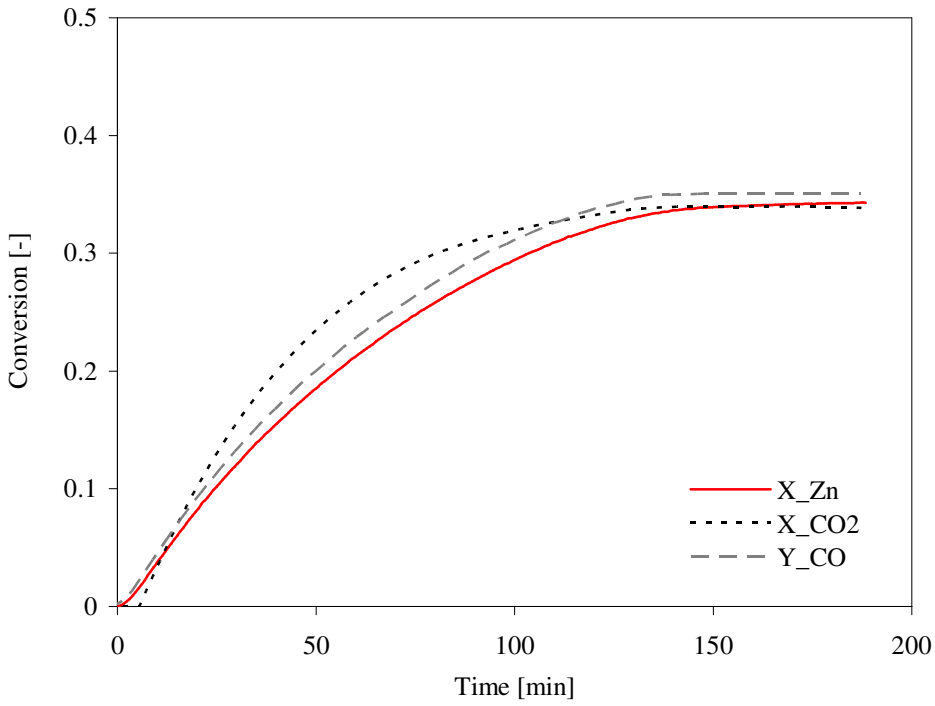


Fig. 7-4: Different reaction extents as a function of time for the isothermal TG run of Zn oxidation with CO2 (6.2 mbar partial pressure) in Argon at 673 K and 1 bar

## 7.6. Results and Discussion

Fig. 7-5 shows the reaction extent as a function of time for the oxidation of zinc dust in the presence of 100% $CO_2$ at 1 bar total pressure. The only changing parameter was the isothermal temperature varied between 673 and 823 K. While at 673 K almost no reaction extent can be observed, at 823 K a reaction extent of 38.3% has been obtained. The reaction rate is characterized by a fast initial increase following a linear trend. This behaviour is typical for a chemical controlled reaction. After ~20 seconds the reaction rate drastically slows down and approaches zero after ~1 min from the beginning of $CO_2$ injection and leads to an incomplete reaction. Based on the previous studies it is believed that during the initial fast reaction a growing layer of zinc oxide starts to enclose the zinc particles. This layer then acts like a barrier and the reacting species has to diffuse through the layer. Obviously the diffusion is immediately almost completely prevented by the layer because further reaction becomes extremely slow. While an increase in temperature seems to extend the reaction controlled part and thus leads to higher reaction extents, the diffusion controlled part experiences almost no change when temperature is increased.

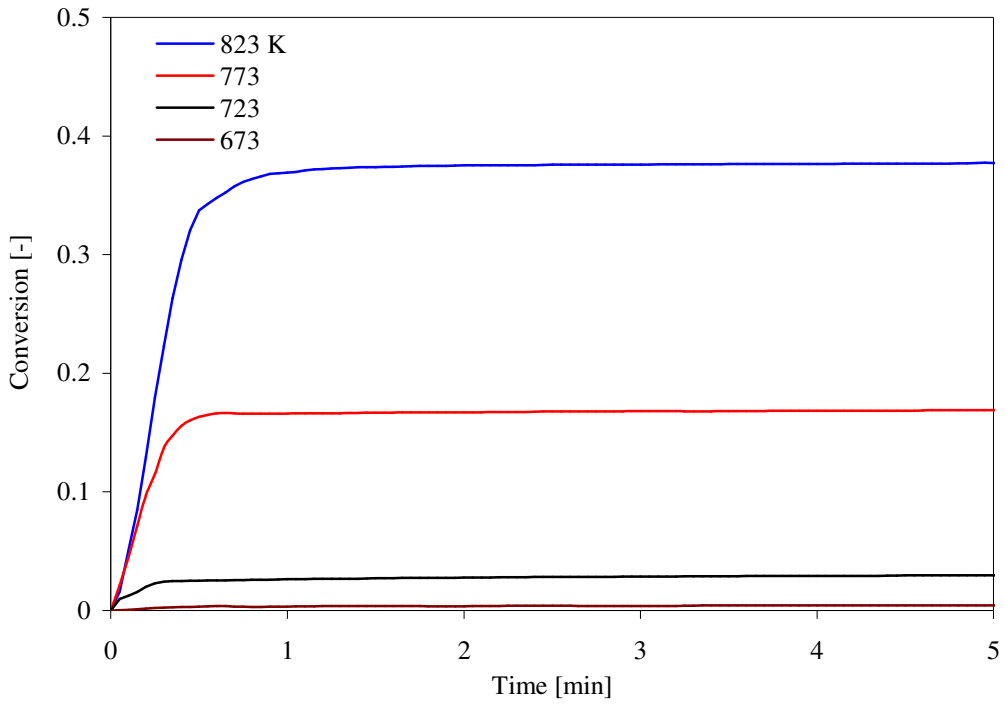


Fig. 7-5: Reaction extent as a function of time, obtained by isothermal TG runs with 100% $CO_2$ and with temperatures in the range of 673 – 823 K.

Fig. 7-6 shows the reaction extent as a function of time for the oxidation of zinc dust in the presence of ~1% $CO_2$ at 1 bar total pressure (partial pressure of $CO_2$ was varying in the range of 5.7-10.6 mbar). The isothermal temperature was varied between 623 and 723 K. Again a fast initial increase, almost linear and presumably reaction controlled, passing over into a very slow diffusion controlled reaction regime can be observed. Using only ~1% $CO_2$, a remarkable reaction extent can be observed already at lower temperatures, above 623 K. Compared to the experiments using 100%

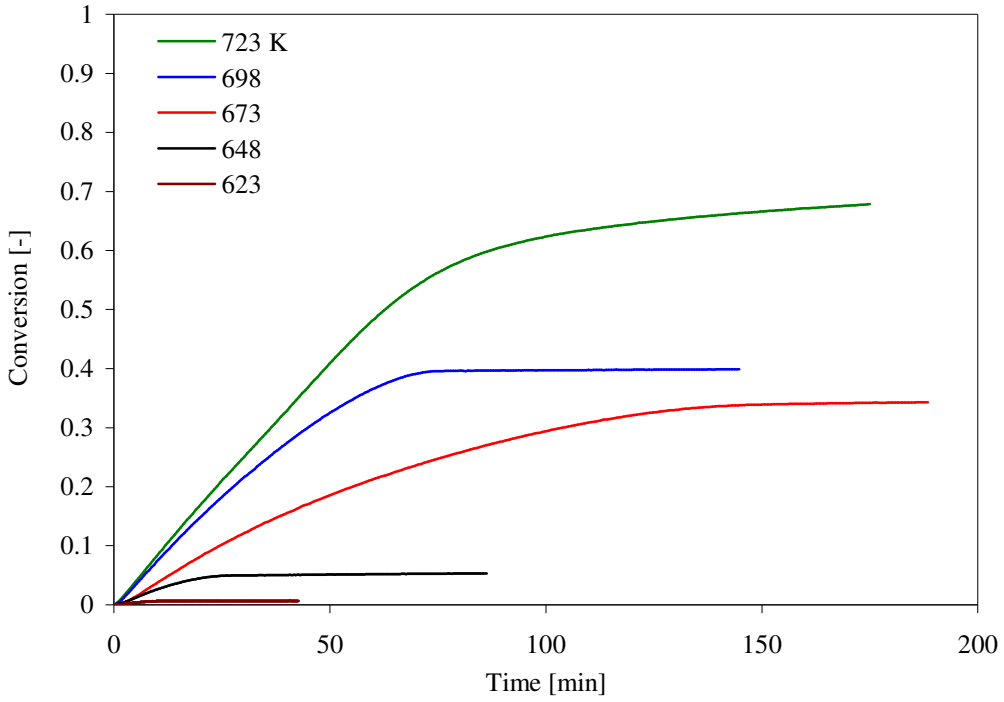


Fig. 7-6: Reaction extent as a function of time, obtained by isothermal TG runs with ~1% $CO_2$ and with temperatures in the range of 623 – 723 K.

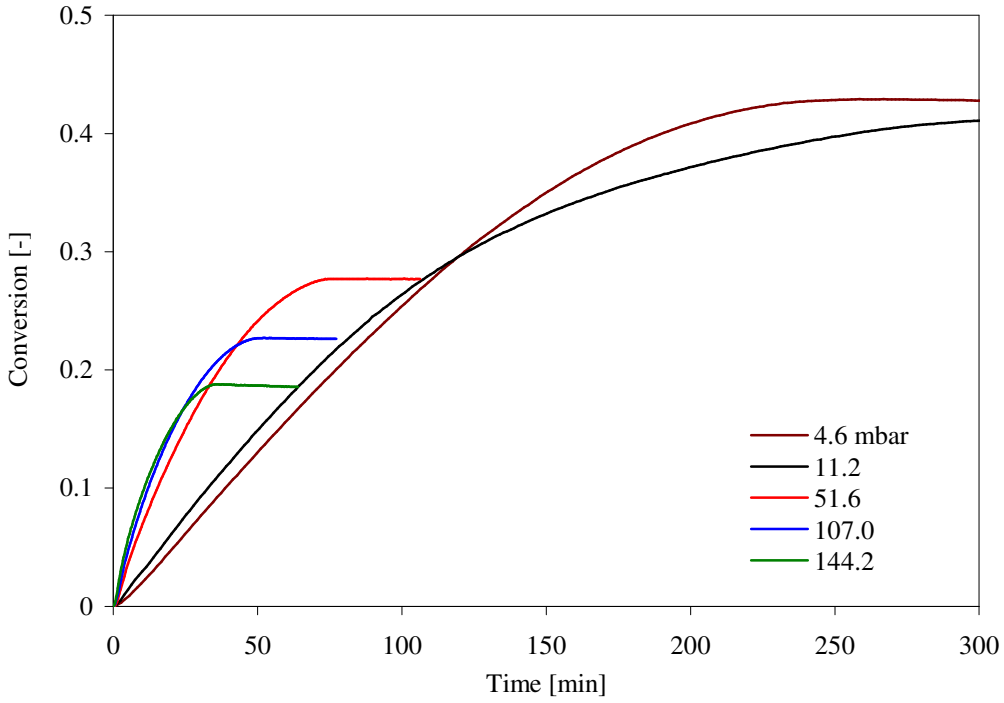


Fig. 7-7: Reaction extent as a function of time, obtained by isothermal TG runs at a temperature of 673 K and with various $CO_2$ partial pressures.

$CO_2$, the oxidation occurs slower but reaches a higher reaction extent when using only 1% $CO_2$. E.g. at a temperature of 723 K the reaction rate was $3.2 \cdot 10^{-3}$ $min^{-1}$ and a maximal reaction extent of 67.9% was achieved whereas at the same temperature the experiment with 100% $CO_2$ showed a reaction rate of $3.4 \cdot 10^{-2}$ $min^{-1}$ and a maximal reaction extent of 3.7%. So far it can be concluded that the lower the initial reaction rate the higher will be the overall reaction extent. This fact can also be observed in Fig. 7-7 where the conversion is plotted as a function of time for different $CO_2$ partial pressures. All the experiments were carried out at an isothermal temperature of 673 K. The highest reaction extent, 42.9%, was achieved with the lowest $CO_2$ partial pressure, 4.6 mbar, corresponding to a $CO_2$ concentration of ~0.5% in the reactant gas. With increasing $CO_2$ partial pressure an increase in the initial reaction rate coupled with a decrease in the overall reaction extent can be observed.

The influence of $CO_2$ partial pressure on the initial reaction rate k is shown in Fig. 7-8. k corresponds to the average slope of the reaction controlled regime, i.e. the fast initial reaction. The regression line shows a dependence on $CO_2$ partial pressure of an order of 0.395 supported by a high coefficient of determination of $R^2 = 0.99$. The found dependence on $CO_2$ partial pressure is comparable with the half order dependence found by Ernst when using $H_2O$ as reducing agent. The intermediate order furthermore suggests that the rate must be reaction limited e.g. by dissociation of the reactant gas on the Zn/ZnO surface before reaction [35].

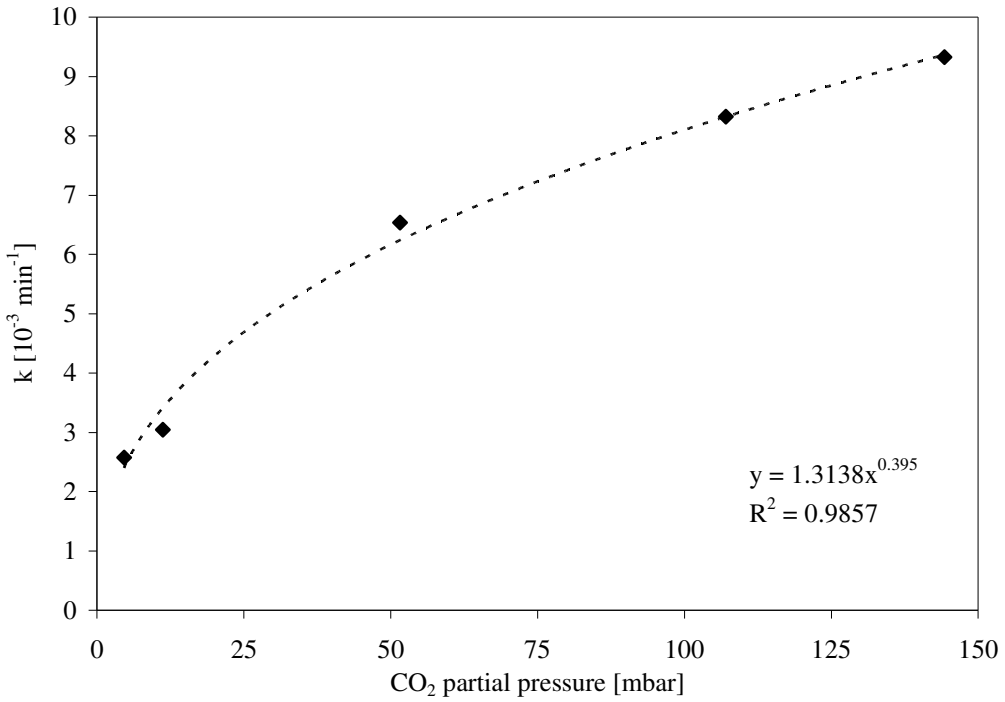


Fig. 7-8: Reaction rate as a function of $CO_2$ partial pressure, obtained by isothermal TG runs at a temperature of 673 K and with various $CO_2$ partial pressures.

The results from the BET analysis are presented in Tab. 7-1 for commercial Zn dust and for various products obtained from isothermal TG runs at 673 K and with various $CO_2$ partial pressures. The

specific surface area was calculated by using the BET equation. Micropore and mesopore volumes were determined by the t-plot empirical method. Both, reactant and products, show a small specific surface area, zero microporosity and only a small amount of mesopore volume. The initial Zn as well as the produced ZnO are clearly a nonporous solid with a macro external surface. This result confirms the formation of a dense ZnO layer around the Zn particles which is responsible for incomplete conversion.

| | Sample | $S_{BET}$ [$m^2$/g] | $V_{micro}$ [$cm^3$/g] | $V_{meso}$ [$cm^3$/g] |
|---|---|---|---|---|
| reactant | Zn dust | 5.0 | 0 | 0.0115 |
| products | 11.2 mbar | 3.2 | 0 | 0.0077 |
| | 51.6 mbar | 4.3 | 0 | 0.0111 |
| | 107.0 mbar | 4.0 | 0 | 0.0091 |

Tab. 7-1: Textural characterization of reactant and products obtained by isothermal TG runs at a temperature of 673 K and with various $CO_2$ partial pressures.

As observable in Fig. 7-6 and Fig. 7-7, some experiments, especially when carried out using low $CO_2$ concentrations, show irregularities and variations in the shape of the conversion curves towards the end of the reaction. Szekely and Themelis [39] reported in context with the reduction of iron oxide that such deviations are most likely due to physical phenomena which can either accelerate or decelerate the reaction. For instance cracking or spalling may increase the area of unconverted phase exposed to the reacting gas and accelerate the reaction. And at elevated temperatures recrystallisation or sintering of the outer shell may decrease the number of available passages through which the gas may advance to the unreacted core of the particle.

Various pictures taken by scanning electron microscope (SEM) give evidence of the appearance of cracks and spalling of the shell. Fig. 7-9 shows the commercial zinc dust before reaction. The spherical particles, with particle diameters varying between 0.5 and 7 µm, exhibit either a smooth surface with sporadic spots or a rough surface. The irregularities on the surface are believed to be due to partial oxidation of the zinc surface.

Fig. 7-10 shows oxidised zinc particles obtained from an isothermal TG-run at a temperature of 673 K and with a $CO_2$ partial pressure of 144.2 mbar, corresponding to ~15% $CO_2$ in the reactant gas. The particle surface is characterized by edged mountainous uprisings featuring small slots which remind of the formation of volcanoes. The picture shows clearly the formation of a hollow particle and the appearance of cracks in the outer shell. Furthermore, inside the particle the directional formation of crystals can be observed. Such crystals indicate that at least a part of the ZnO is formed by a gas-gas reaction on a solid surface through nucleation and growth.

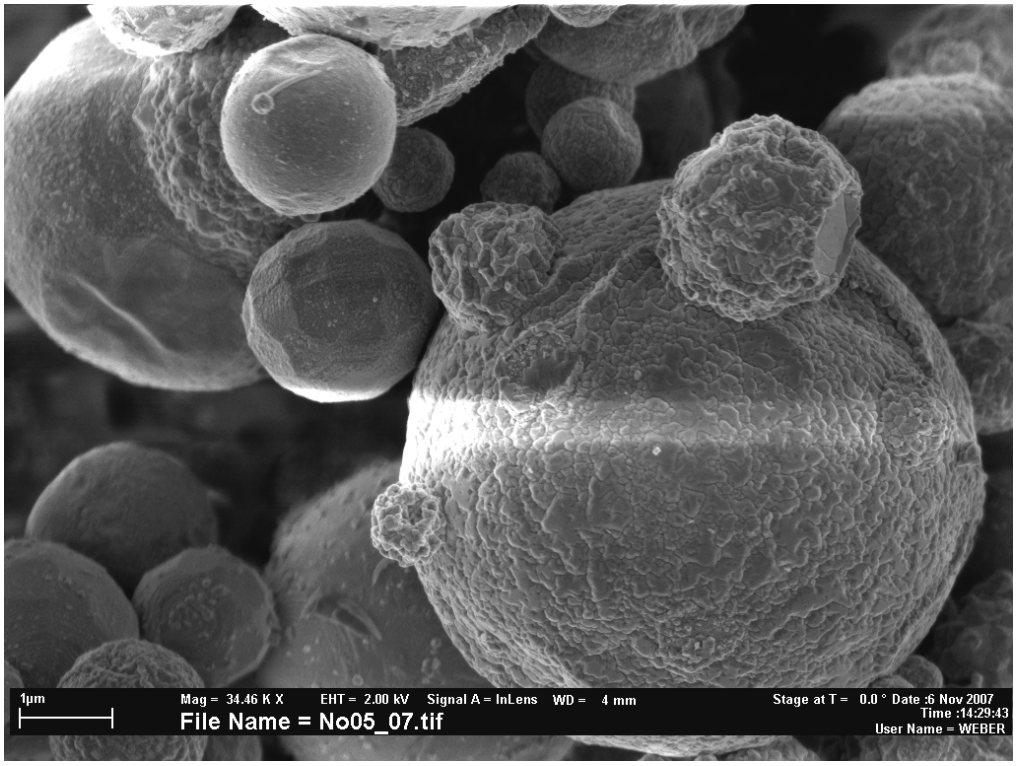


Fig. 7-9: SEM picture of commercial Zn powder

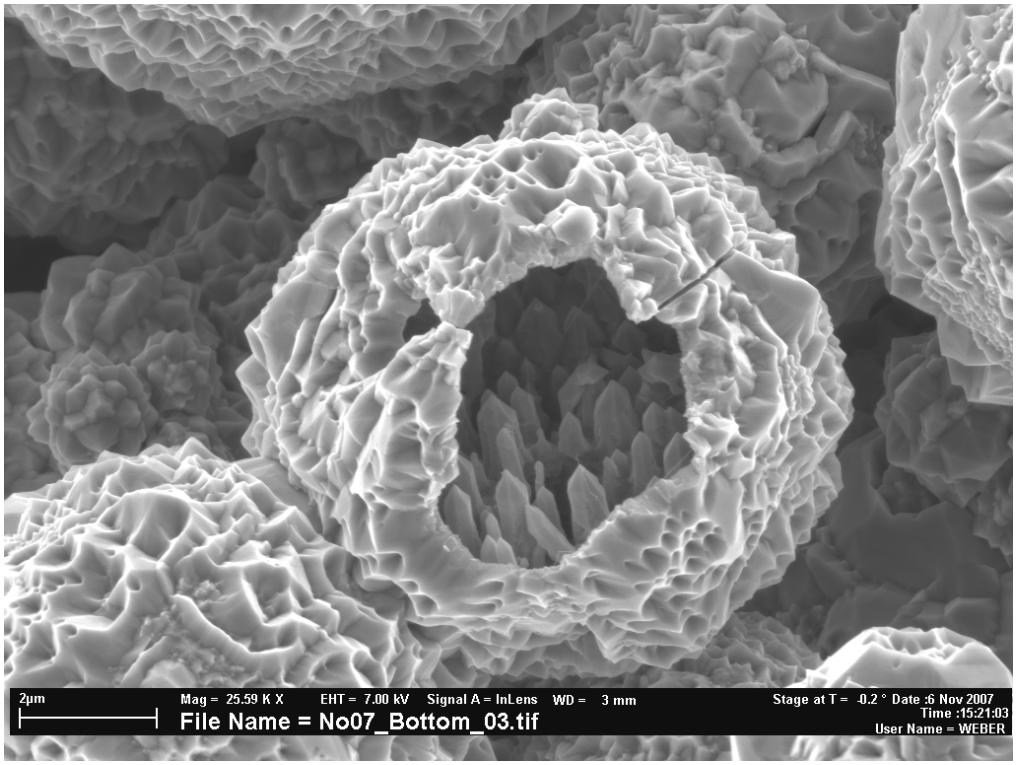


Fig. 7-10: Oxidised particles from the isothermal TG-run at T = 673K and $p_{CO2}$ = 144.2 mbar exhibiting cracks and crystal formation inside the particle.

In Fig. 7-11 and Fig. 7-12 the influence of temperature is shown. The pictures show the oxidised zinc dust after the isothermal TG-runs with 1% $CO_2$ at a temperature of 648 and 723 K. At a low temperature (Fig. 7-11), single hollow particles with partly oxidised surface can be observed. At higher temperature (Fig. 7-12), the particles are more oxidised and therefore have a thicker and more distinct ZnO shell. Furthermore, the particles stick together and build agglomerates. At higher temperatures more gaseous Zn will be formed which may, freely or partly adsorbed, move around (e.g. by surface diffusion processes). The Zn atoms then react with $CO_2$ on the Zn/ZnO surface and form ZnO crystals.

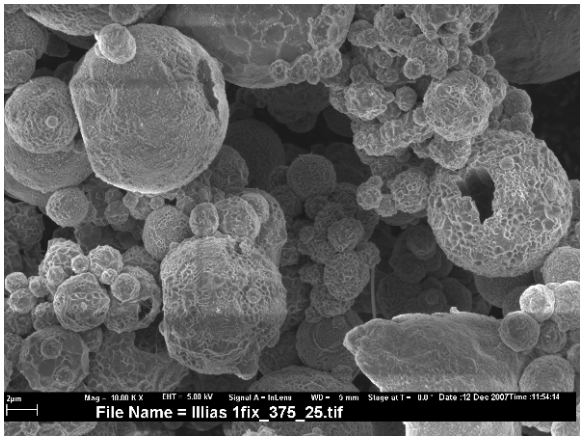


Fig. 7-11: Oxidized Zn at T = 648 K and ~1% $CO_2$

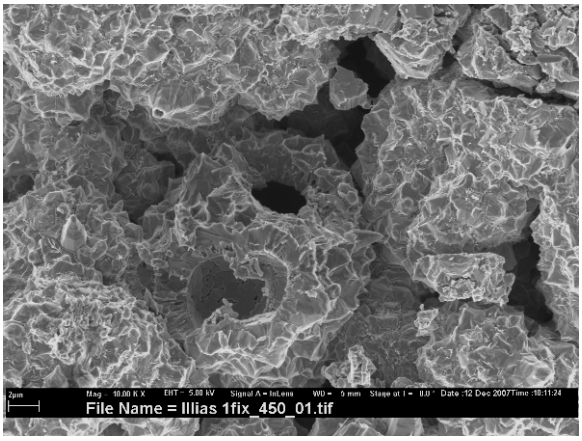


Fig. 7-12: Oxidized Zn at T = 723 K and ~1% $CO_2$

The influence of $CO_2$ partial pressure is represented by Fig. 7-13 to Fig. 7-16. The pictures show the products obtained with an isothermal temperature of 673 K and with a $CO_2$ partial pressure of 4.6 mbar (upper line) and 144.2 mbar (lower line), respectively. As all the experiments were carried out at the same temperature they are supposed to have equal conditions concerning the mobility of Zn atoms, i.e. solid bulk diffusion or gas diffusion processes of sublimated Zn atoms. Nevertheless, one can clearly observe that at lower $CO_2$ partial pressure the particle surface exhibits fine crystals and needles up to several micrometers long. However at higher $CO_2$ partial pressure the oxidised particles show a smoother ZnO surface. It is therefore believed that higher $CO_2$ partial pressures lead to immediate conversion of the Zn surface or sublimated Zn atoms. Once the surface is covered by ZnO, the sublimation of Zn atoms is inhibited and further oxidation is only possible by extremely slow bulk diffusion processes. With fewer $CO_2$ molecules available, i.e. at low $CO_2$ partial pressure, the diffusion path length of sublimated Zn atoms increases and allows the formation of ZnO crystals by vapour deposition processes. This leads to an increase of the available reaction surface and increase in overall conversion as it can be observed in Fig. 7-7. Furthermore, at low partial pressure, the samples show different shapes dependent on their position on the crucible in the TG. While the picture taken at the bottom part of the sample (Fig. 7-13) shows single hollow particles with fine crystals on their surface, the picture from the top of the sample is showing needles, bigger crystals and agglomerated particles (Fig. 7-14). It is believed that at low partial pressure and hence higher diffusion path lengths sublimated Zn atoms are carried upwards by the carrier gas argon. This results in a higher Zn gas concentration in the upper part which leads to the formation of needles and agglomerated particles.

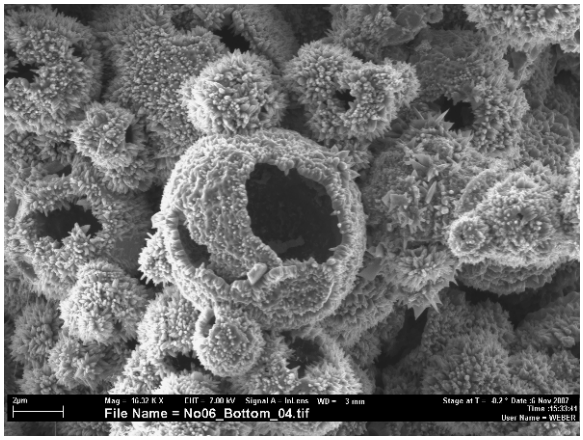


Fig. 7-13: 673 K, $p_{CO2}$ 4.6 mbar, sample bottom

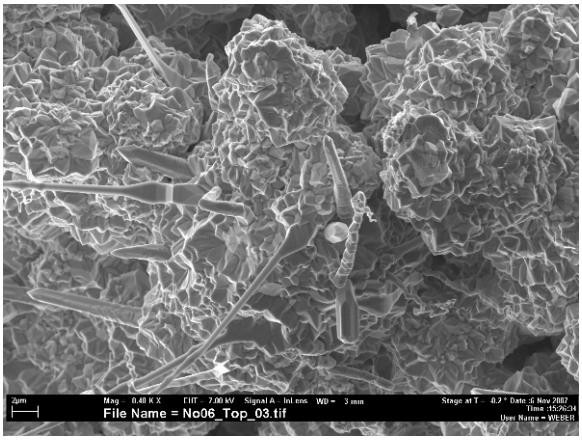


Fig. 7-14: 673 K, $p_{CO2}$ 4.6 mbar, sample top

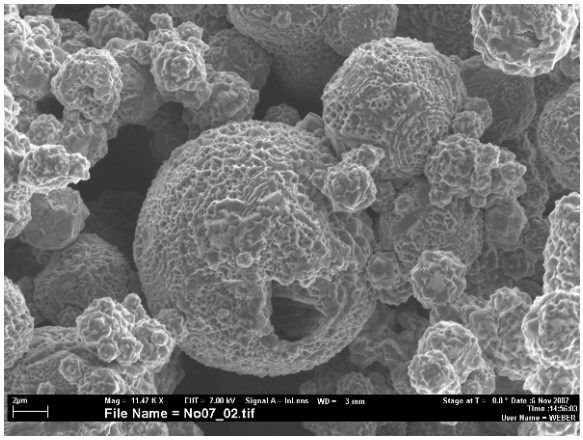


Fig. 7-15: 673 K, $p_{CO2}$ 144.2 mbar, powder

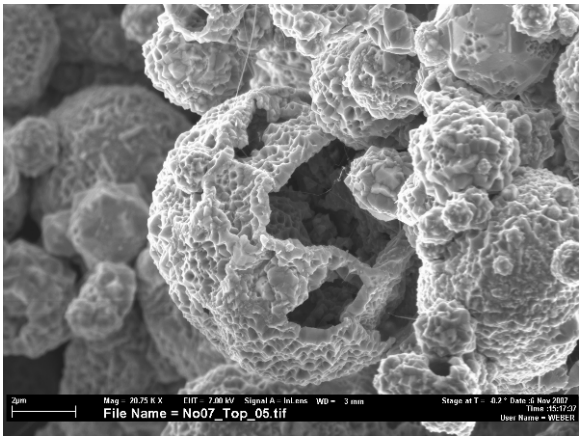


Fig. 7-16: 673 K, $p_{CO2}$ 144.2 mbar, sample top

A comparison of the final Zn conversions revealed, that the ones calculated from the TG results were usually lower than the ones obtained from XRD measurements. As already explained earlier it is believed, that a certain measurement uncertainty occurs from ongoing Zn oxidation after stopping the TG measurement, i.e. during cooling of TG. However, experiments with lower final Zn conversion generally showed a higher relative error as represented in Tab. 7-2 for various experiments. The relative error was calculated according to the definition given in eq. (7.10).

| Sample | $X_{Zn}$ (TG) | $X_{Zn}$ (XRD) | relative error [-] |
|---|---|---|---|
| 4.6 mbar | 42.9 % | 58.1 % | 0.26 |
| 11.2 mbar | 41.2 % | 57.5 % | 0.28 |
| 51.6 mbar | 27.7 % | 41.1 % | 0.33 |
| 107.0 mbar | 22.7 % | 33.3 % | 0.32 |
| 144.2 mbar | 18.7 % | 29.1 % | 0.36 |

Tab. 7-2: Zn conversion measured by TG and XRD and the corresponding relative error for experiments carried out with various $CO_2$ partial pressures and at a temperature of 673 K.

$$\text{relative error} = \frac{X_{Zn}(XRD) - X_{Zn}(TG)}{X_{Zn}(XRD)} \tag{7.10}$$

The increasing relative error with lower final conversions is believed to be a consequence of the XRD measurement. As the penetration depth of the XRD is only several micrometers, the measurement gives an average of the outer surface layer of the particles. While the outer layer is believed to consist mainly of ZnO, there must be unconverted Zn inside the particles, especially in those which don't feature holes and cracks. This unconverted and by ZnO enclosed Zn will only be partly accounted in the XRD measurement in contrast to the TG measurement which is based on the weight change. An increase in the relative error therefore represents an increase of unconverted Zn encased by ZnO and hence a decrease of cracked and hollow particles. This conclusion is supported by the number of hollow particles visible in Fig. 7-13 and Fig. 7-15.

Other phenomena observed by SEM pictures are the formation of big Zn/ZnO particles in the order of ~100 µm (Fig. 7-17). As the isothermal temperature was well above the melting point of zinc, Zn droplets have been formed during heating up in Argon. When $CO_2$ was introduced, the surface of the Zn droplets was immediately oxidized and covered with ZnO. Vaporization of the residual Zn core may lead to an increase in pressure inside the particles which provokes the formation of cracks and holes in the ZnO shell. Some particles seem to have been collapsed as a consequence of the thin ZnO shell compared to the particles size. The same behaviour has already been reported previously by Gao and Wang [37].

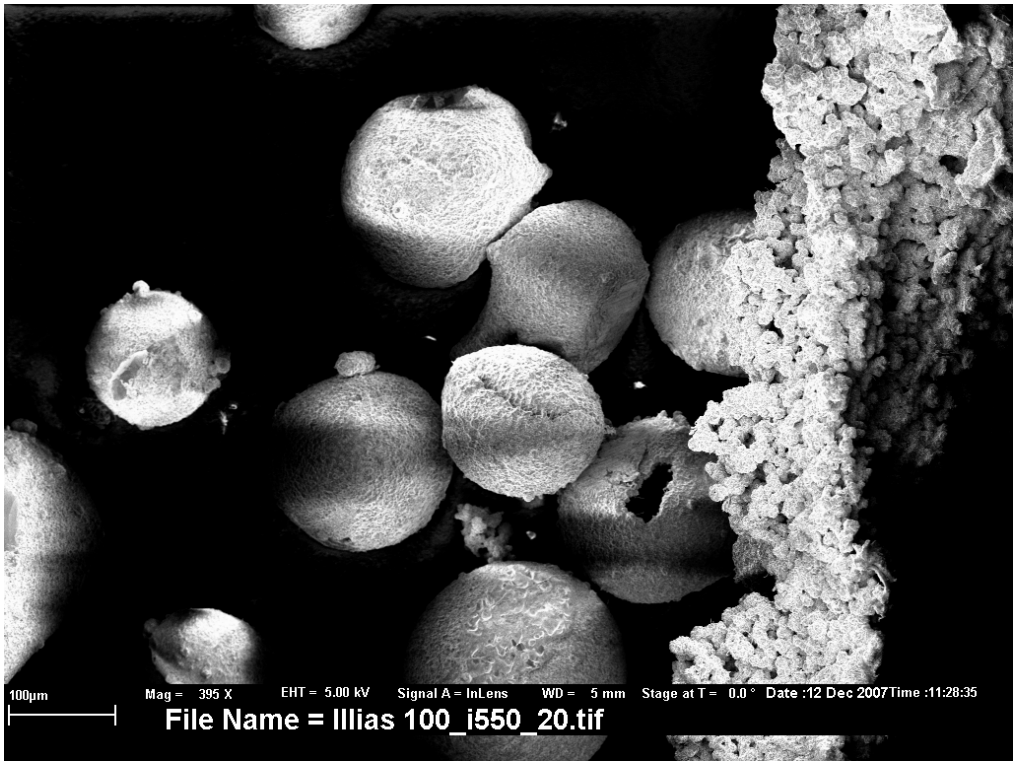


Fig. 7-17: Formation of Zn droplets and simultaneous oxidation at T=823 K, 100% $CO_2$

Concerning the oxidation of Zn with $CO_2$ in the temperature range of 623 – 823 K, the following observations have been made so far:

- Zn particles are initially oxidised at the surface leading to a ZnO shell, encasing unconverted Zn.
- Some particles feature cracks and holes in the ZnO shell through which unconverted Zn is made accessible.
- Above 673 K, gas diffusion or surface diffusion processes through sublimated or adsorbed Zn atoms dominate over slow bulk diffusion processes and remarkably increase the reaction rate and final conversion.
- At lower $CO_2$ partial pressure, the Zn atoms show higher mobility and lead to the formation of ZnO crystals and needles.
- At higher $CO_2$ partial pressure, the Zn atoms are immediately converted to ZnO leading to a compact ZnO shell and unconverted Zn.
- Cracking of particles is a discrete process and may be provoked by increasing zinc partial pressure inside the particles due to sublimation of encased Zn. Thereby a local temperature increase due to the exothermic conversion of Zn to ZnO may shift temporarily the equilibrium from solid to gaseous zinc.

A schematic model of the observed phenomena explaining the formation of hollow ZnO shells is given in Fig. 7-18. Picture 1 shows an initial zinc particle surrounded by $CO_2$. In picture 2 small ZnO nuclei are formed on the Zn surface. The nuclei then grow rapidly in different directions depending on the $CO_2$ partial pressure until they form a closed ZnO shell.

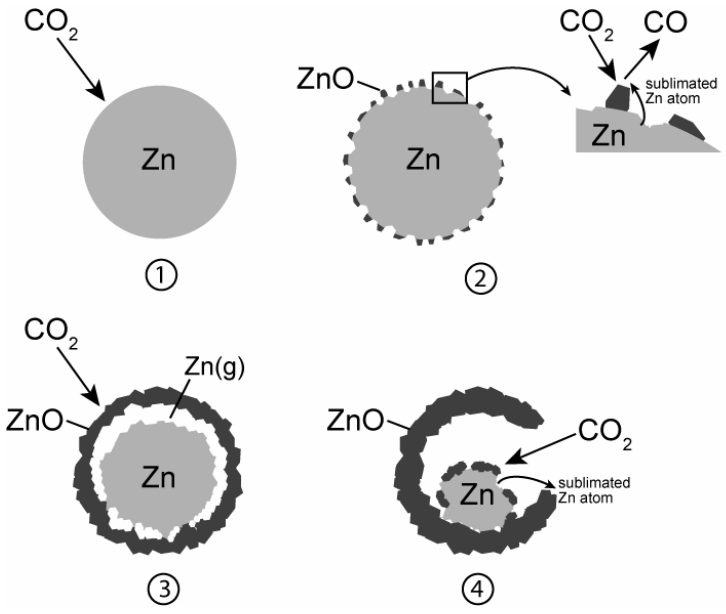


Fig. 7-18: Schematic model for the proposed zinc oxidation mechanism through gas and surface diffusion of sublimated zinc atoms.

From picture 3 it becomes clear, that once a ZnO shell has formed around the remaining Zn particle, further oxidation is only possible by slow bulk diffusion processes. For particles where cracks in the shell occur, as shown in picture 4, the remaining Zn will be accessible without bulk diffusion and a much faster oxidation will be possible.

An appropriate model describing the observed phenomena is given with the crackling core model (CCM) by Park and Levenspiel [40]. It is basically an extension of the shrinking core model and views the particle to be initially nonporous. Cracking and fissuring leads to the formation of a porous and grainy structure which is easily accessible (no diffusional resistance) and which then reacts away to final product according to the shrinking core model. The CCM is a two parameter model represented by the characteristic times, $\tau_{core}$ and $\tau_{grain}$:

$\tau_{core}$ = time for the non-porous material to be completely converted to grainy porous solid
$\tau_{grain}$ = time for complete conversion of the solid

A representative example of $\tau_{core}$ and $\tau_{grain}$ is given in Fig. 7-19 for the TG run carried out at an isothermal temperature of 723 K and with ~1% $CO_2$. Here, $\tau_{core}$ represents the time of regime 1, the initial fast reaction which is chemically controlled and attributed to the time, during which unconverted zinc and hence reaction surface is easily available. This may be the case due to crackling and spalling of the ZnO layer around the particles or due to intermediate gaseous zinc depositing on the ZnO shell and thus available for reaction. The conversion reached by this first reaction mechanism may also be represented by $X_i$ as indicated in Fig. 7-19.

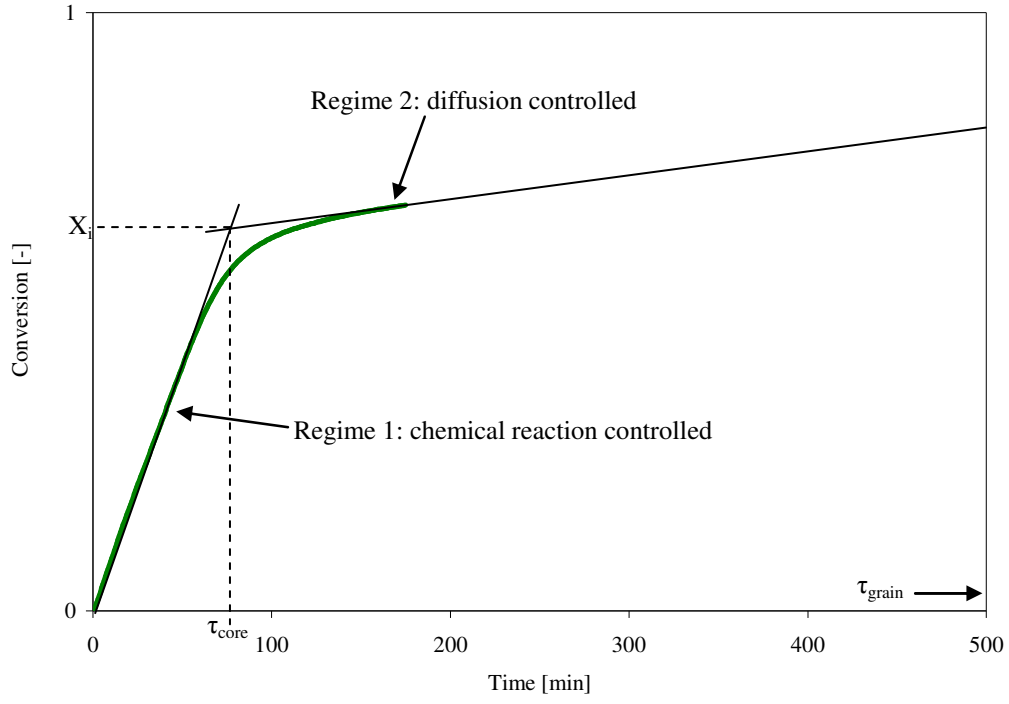


Fig. 7-19: Exemplary representation of the characteristic times, $\tau_{core}$ and $\tau_{grain}$, describing the CCM.

The following second reaction mechanism in regime 2 is much slower and diffusion controlled due to the compact ZnO layer formed around unreacted Zn. The time to reach full conversion is then given by $\tau_{grain}$. However, it is obvious that $\tau_{grain}$ is much bigger than $\tau_{core}$ and especially at low temperatures and high $CO_2$ partial pressures (see Fig. 7-5 to Fig. 7-7) $\tau_{grain}$ tends toward infinity. For this extreme, where $\tau_{grain} \to \infty$, the conversion follows the shrinking core model (SCM) reaction control to a final conversion less than 100% [41].

It has to be mentioned here, that Park and Levenspiel assumed for the CCM, that an initially non-porous solid is steadily converted into a porous structure of grains. In the case of high temperature zinc oxidation (623 – 823 K) this is only partly the case for a single particle, because cracking of the shell seems to take place as a discrete process: either the shell cracks or it doesn't. However, as we are not looking on a single zinc particle but on zinc powder consisting of many particles, many discrete actions will superimpose and form a continuous process. The CCM seems therefore to be a good approximation to describe the oxidation of zinc powder as it takes into account an increase of available reaction surface through cracking. E.g., it is able to explain a final conversion less than 100%. However, for an exact description of the whole process, gas diffusion and surface diffusion of sublimated Zn atoms as well as the conditions for cracks have to be taken into account. This will of course lead to a rather complicate model.

For the efficient splitting of $CO_2$ via Zn oxidation, only the fast initial reaction within time $\tau_{core}$ is of interest. The first regime is hence modelled with the chemical reaction controlled SCM as suggested by Levenspiel in the case where $\tau_{grain} \to \infty$. The conversion expression is then given by eq. (7.11).

$$1-\left(1-X\right)^{1/3} = k \cdot t \tag{7.11}$$

$X$ represents the conversion, $t$ is the time and k is the rate constant given by an Arrhenius-type relationship according to eq. (7.12), where $k_0$ is the reaction rate constant, $E_a$ the activation energy, $R$ the ideal gas constant and $T$ the temperature.

$$k = k_0 \cdot e^{-E_a/RT} \tag{7.12}$$

The Arrhenius plots obtained from the isothermal TG data with 1% $CO_2$ and 100% $CO_2$ by applying the SCM to the first reaction regime are shown in Fig. 7-20 and the corresponding Arrhenius kinetic parameters are represented by Tab. 7-3.

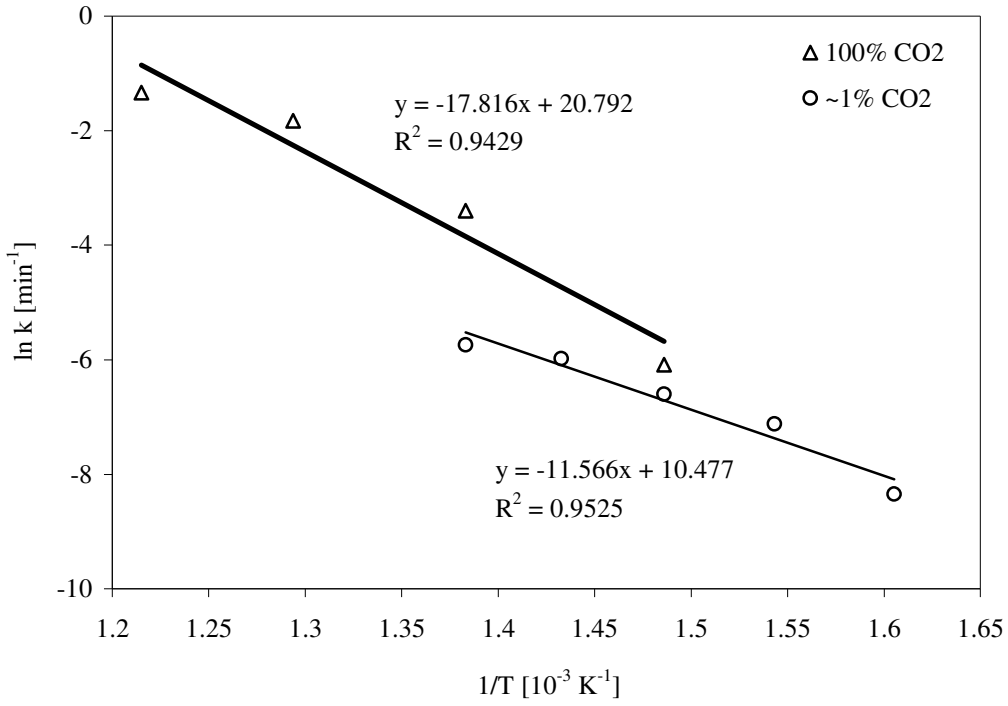


Fig. 7-20: Arrhenius plots of the isothermal experiments using 100% CO2 (triangles) and ~1% CO2 (circles) obtained by applying the reaction controlled SCM.

| $CO_2$ percentage in the reaction gas | $E_a$ [kJ·mol$^{-1}$] | $k_0$ [min$^{-1}$] | $R^2$ [-] |
|---|---|---|---|
| 1% $CO_2$ | 96.1 | $3.5 \cdot 10^4$ | 0.9525 |
| 100% $CO_2$ | 148.1 | $1.1 \cdot 10^9$ | 0.9429 |

Tab. 7-3: Arrhenius kinetic parameters for the oxidation of zinc at 1 bar with 1% and 100% $CO_2$ respectively.

The correlation coefficient $R^2$ is given by eq. (7.13), where $x$, $y$ are the experimental and $\bar{x}$, $\bar{y}$ the calculated values respectively.

$$R^2 = \frac{\left[\sum (x-\bar{x})(y-\bar{y})\right]^2}{\sum (x-\bar{x})^2 \sum (y-\bar{y})^2} \tag{7.13}$$

For the experiments performed in 100% $CO_2$, an apparent activation energy of 148.1 kJ/mol has been found. For the oxidation of zinc with $CO_2$ no other activation energy has been found so far and therefore a comparison is not possible at this point. For the oxidation of zinc with water vapour under similar conditions, most activation energies are reported to be between 95 – 145 kJ/mol [35]. For the experiments carried out with only 1% $CO_2$, corresponding to a $CO_2$ partial pressure of 1 mbar, a lower apparent activation energy of 96.1 kJ/mol has been found. As shown by the SEM pictures, a low $CO_2$ partial pressure resulted in the formation of ZnO crystals and needles because

the mobility of sublimated or adsorbed Zn atoms is higher. A shift from slow bulk diffusion processes to surface and gas diffusion processes is therefore believed to be the reason for a decrease in the activation energy at lower $CO_2$ partial pressure. A decrease in activation energy has also been reported when using smaller particles [35]. For smaller particles it is known that evaporation and sublimation is facilitated due to the Kelvin effect [42]. This may provoke the shift from bulk diffusion to surface and gas diffusion processes at even lower temperatures and therefore result in much lower activation energies.

The results of the kinetic modelling are shown in Fig. 7-21 for the data obtained with 100% $CO_2$ and in Fig. 7-22 with 1% $CO_2$. The modelled data (solid line) fit fairly well to the experimental data (Markers) and support the validity of the chosen model.

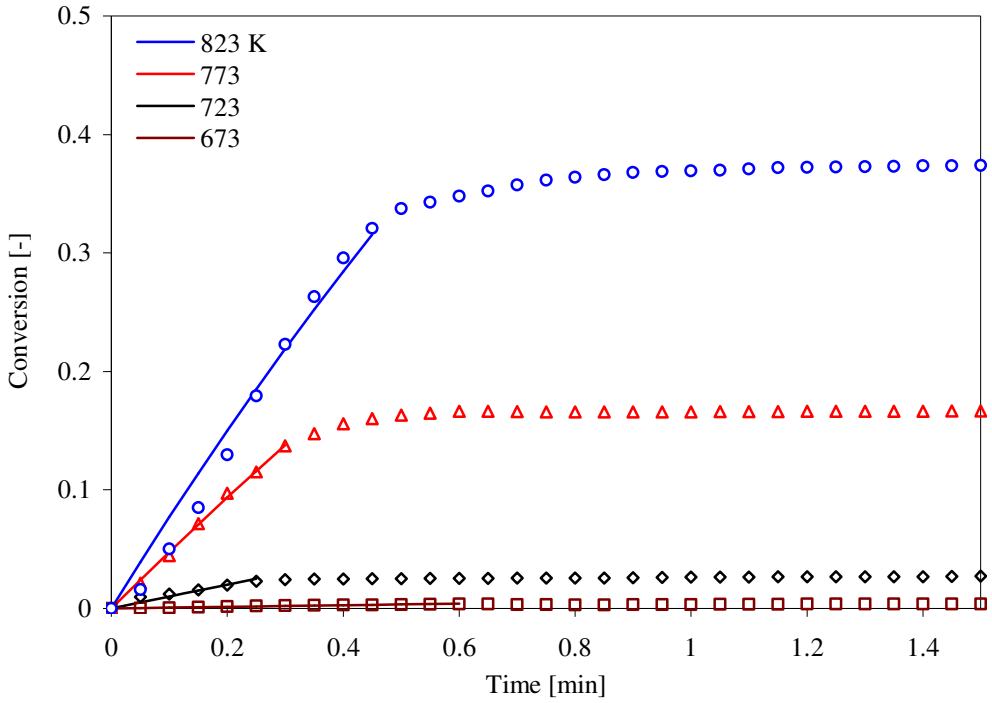


Fig. 7-21: Comparison of the experimental data obtained by isothermal TG runs with 100% $CO_2$ (Markers) and the results obtained form the kinetic modelling using the reaction controlled SCM (solid lines).

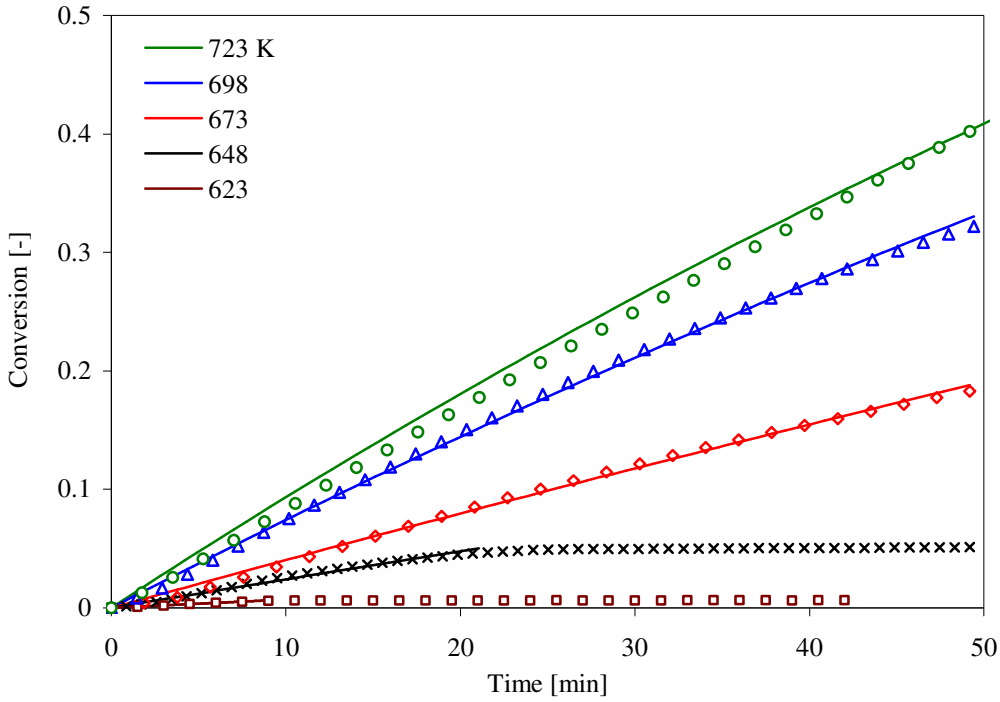


Fig. 7-22: Comparison of the experimental data obtained by isothermal TG runs with ~1% CO2 (Markers) and the results obtained form the kinetic modelling using the reaction controlled SCM (solid lines).

# 8 Reactor Study

For the study of a possible reactor suitable for the $CO_2$ splitting with zinc, an experimental campaign with a hot-wall aerosol reactor has been performed. The same reactor was already used by Ernst et al. for the production of hydrogen by in-situ Zn aerosol formation and hydrolysis [43]. It was originally designed by Ly and Weiss [44] and further improved by Savi and Rusconi [45]. The basic idea is the production of Zn nanoparticles by rapid cooling of Zn vapour. Nanoparticles exhibit a big surface to volume ratio and hence offer an increased reaction surface. By increasing the reaction surface, more Zn will be able to react before it is enclosed by ZnO. This will lead to a faster oxidation and an increased overall Zn conversion.

## 8.1. Setup

The aerosol reactor consists of a lower and an upper part which are merged together by a standardized conical grinding and vertically fixed on a rack. The lower part consists of a 590 mm long quartz tube. The upper part with a total length of 1000 mm is built together by three concentric quartz tubes of different diameters and lengths which are sealed by flanges. On its top a glass fibres filter (Whatman GF/A, diameter 150 mm) is placed in a stainless steel filter-holder. Two furnaces (furnace 1: Carbolite, VST 17/250, furnace 2: Carbolite VST 12/400) which are separated by a variable distance, enclose the quartz tube and allow to set two different temperatures: $T_E$ in the evaporation zone and $T_R$ in the reaction zone (see Fig. 8-1). Additionally, the temperatures in the evaporation zone and reaction zone were measured with two thermocouples (K-type). The evaporation zone contains a ceramic crucible which is filled with zinc and standing on a balance (Mettler-Toledo) inside a hermetically sealed balance box. An electric engine which is installed inside the balance box allows shifting the crucible up and down. An Argon-flow, controlled by a mass flow controller (Bronkhorst EL-Flow), is introduced at the bottom of the balance box and directed upwards to carry evaporated zinc to the cooling zone, where the zinc vapour is cooled down by ambient air. A reactant gas flow is introduced at the top of the reactor and flowing in the outer annulus through furnace 2, where it is mixed with the Zn laden carrier gas in the mixing area. The mixture is then streaming in the innermost quartz tube through the reaction zone where the reaction is taking place. Finally the particles are collected in the filter, whereas the gas-flow is measured by a flow meter (Kobold flow meter) and analysed with a gas chromatograph (two-channel Varian Micro GC, equipped with Molsieve-5A and Poraplot-U columns). For the data acquisition a PC is connected to the balance and to a message device (Delphin Technology, TopMessage) to record zinc evaporation, temperatures and outlet gas flow.

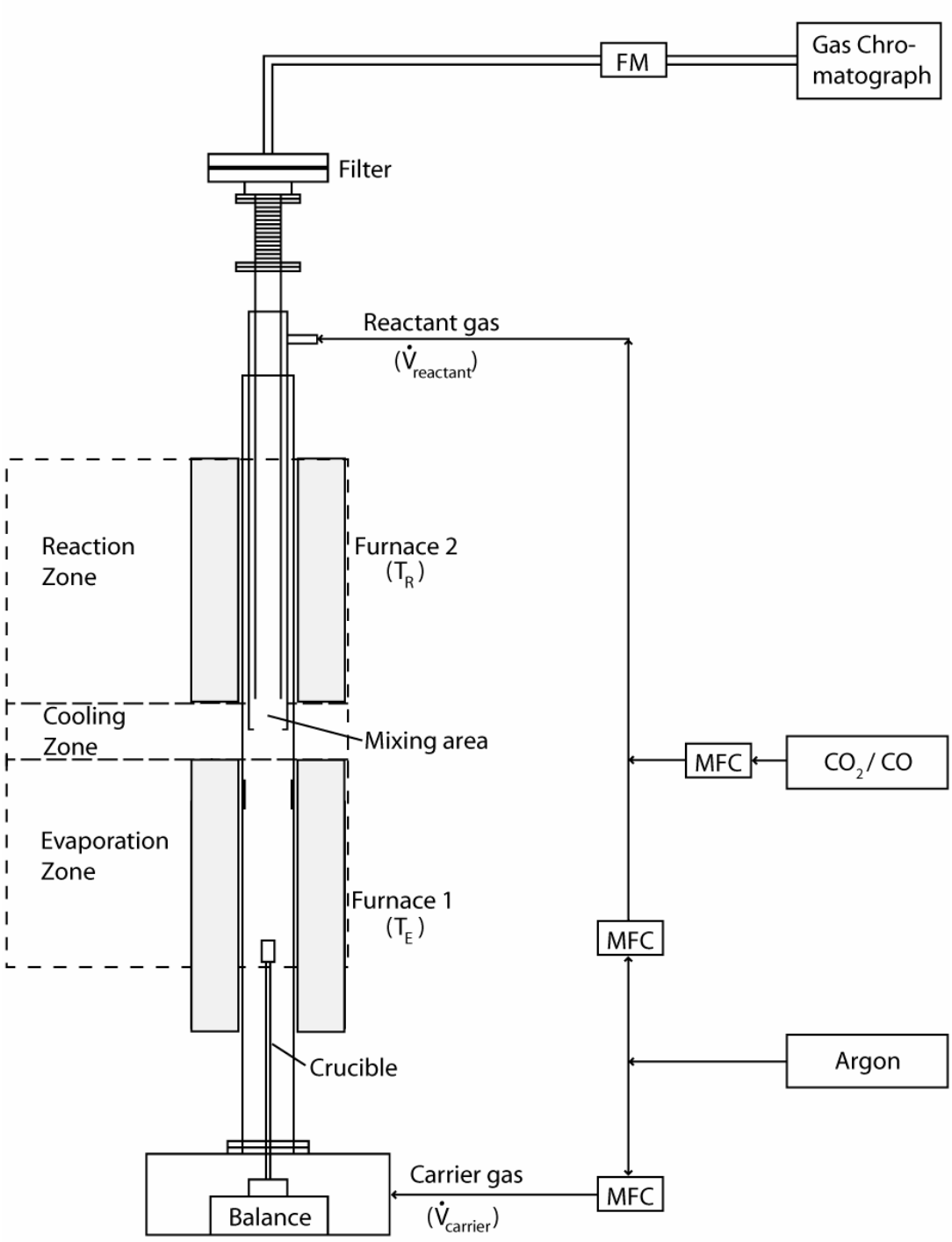


Fig. 8-1: Schematic setup of the reactor

## 8.2. Parameters

For the experiments carried out in the aerosol reactor, the following fixed parameters have been set.

- Sample: Zinc granular (Sigma-Aldrich, -30+100 mesh, 99%)
- Reactant gas: CO2 (Pangas 4.5, ≥ 99.995%) or CO (Messer 4.7, ≥ 99.997%)
- Carrier gas: Argon (Messer Schweissargon, ≥ 99.996%)

- Cooling zone length: 5 cm
- Reactant gas flow $\dot{V}_{\text{reactant}}$: 1 l/min
- Carrier gas flow $\dot{V}_{\text{carrier}}$: 2 l/min
- Total pressure: 1 bar
- Evaporation zone furnace temperature $T_E$: 1123 K
- Reaction zone furnace temperature $T_R$: 773 K

The only parameter varied was the $CO_2$ concentration in the reactant gas and expressed in terms of $CO_2$:Zn(g) stoichiometry:

- Stoichiometry $CO_2$:Zn(g): 0.41 – 32.14

## 8.3. Procedure

A sample of 2 grams granular zinc was placed in the crucible. The quartz tubes were mounted together with the flanges and seal rings. A glass-fibre filter was weighted and placed into the filter-holder on top of the reactor. After having sealed connecting tubes with sealing- and tension-rings, the whole reactor was flushed with ~5 l/min argon for approximately 1 hour. With the GC it has been ensured that the remaining oxygen content was below 40 ppm. The carrier gas flow and reactant gas flow were then set to the right value and composition, and the evaporation zone and reactant zone were heated up to the desired value. Once gas flows and temperature stabilized, the balance was set to zero and the crucible was shifted up into the evaporation zone with the electric engine. Weight loss, temperatures, outlet gas flow and composition were recorded with the PC. When no more weight loss and CO in the outlet gas were registered, the reactor was cooled down to ambient temperature in pure argon in order to prevent further oxidation or reaction of the products. Once the reactor was cooled down, it was disassembled and samples were scraped off from the reactor walls at different positions. The glass-fibres filter was weighted a second time in order to calculate the amount of deposits on the filter. The particles were then collected for analysis by SEM (SmartSEM, Carl Zeiss Supra 55VP) and XRD (Philips XPert-MPD powder difractometer). Finally the quartz glass tubes and the ceramic crucible were cleaned in a 20%-hydrochloric acid solution.

## 8.4. Observations

A temperature profile along the centreline of the reactor was measured in pure Argon and with the usual parameters ($\dot{V}_{\text{carrier}}$ = 2 l/min, $\dot{V}_{\text{reactant}}$ = 1 l/min, $T_E$ = 1123K, $T_R$ = 773 K) with a K-type thermocouple (Fig. 8-2). In the evaporation zone (furnace 1) the temperature sharply increases up to a maximum of 1100 K before cooling down to 760 K in the mixing area. In the first half of the reaction zone (furnace 2), the temperature remains fairly stable around 770 K and then drops off to ambient temperature. For the zinc granules in the crucible an average evaporation temperature of 1030±6 K has been measured which led to an average zinc evaporation rate of 44±3 mg/min.

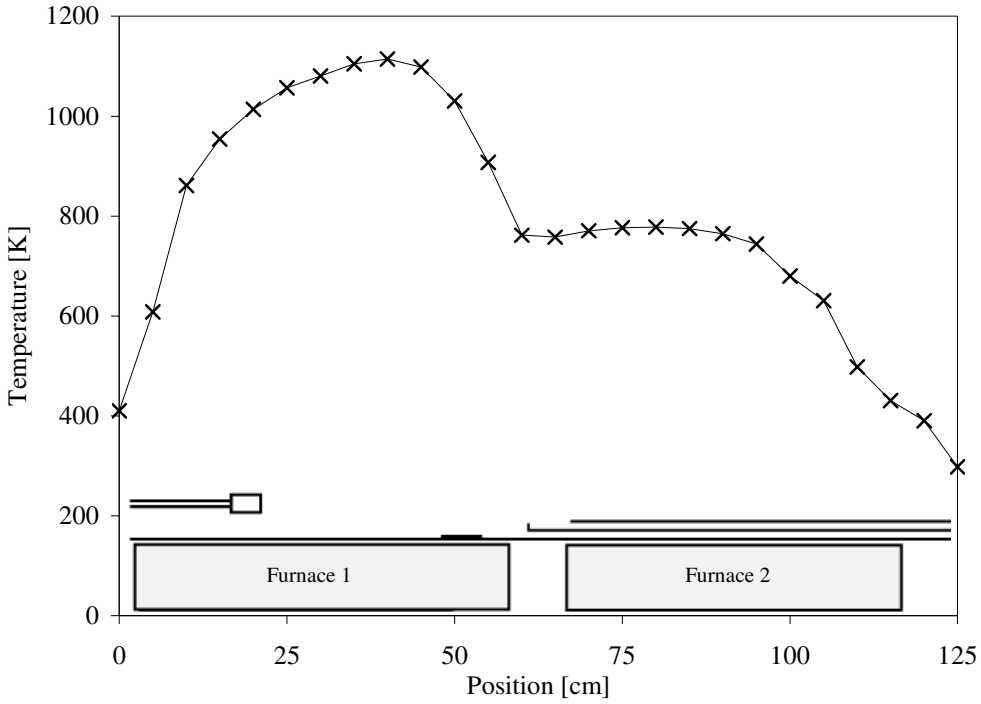


Fig. 8-2: Temperature profile along reactor centreline with corresponding position in the reactor ($\dot{V}_{carrier}$ = 2 l/min, $\dot{V}_{reactant}$ = 1 l/min, $T_E$ = 1123K, $T_R$ = 773 K)

A typical example of an experimental run performed in the aerosol reactor is given in Fig. 8-3. The solid lines are representing the concentration of Zn(g), $CO_2$ and CO in mol/min. The dotted lines give the accumulated values in mol. The $CO_2$ concentration initially set to $6.8 \cdot 10^{-4}$ mol/min is remarkably decreasing once Zn evaporation is taking place. At the same time CO production can be observed, which corresponds to the consumed amount of $CO_2$ and indicating, that the reaction is taking place according to eq. (3.2). Zn evaporation is characterized by a sharp increase within the first 10 min upon introduction of the crucible into the evaporation zone due to heating up of the zinc to the evaporation zone temperature. During evaporation time, approximately 50 min, a slight decrease can be observed probably due to oxidation of residual oxygen right in the crucible, which then increases diffusion resistance limiting Zn evaporation. In the given example, an average zinc concentration of $6.4 \cdot 10^{-4}$ mol/min has been measured resulting in a $CO_2$:Zn stoichiometry of 1.06. After zinc evaporation has stopped, a sharp decrease in $CO_2$ consumption and CO production is visible. However, an ongoing oxidation for another 40 min is clearly observed. It is believed, that during the experiments, Zn deposits on the reactor wall near the reaction zone and is then subsequently oxidised. Generally, white hard deposits consisting of 100% ZnO (measured by XRD) have been observed in the mixing area and lower part of the reaction zone. In the upper part of the reaction zone where the temperature is lower and above, grey deposits consisting of 100% Zn have been found. It is believed that the deposits in between, where the temperature is low enough for zinc to condensate on the walls, but still high enough for fast oxidation, are responsible for the ongoing oxidation after the end of Zn evaporation.

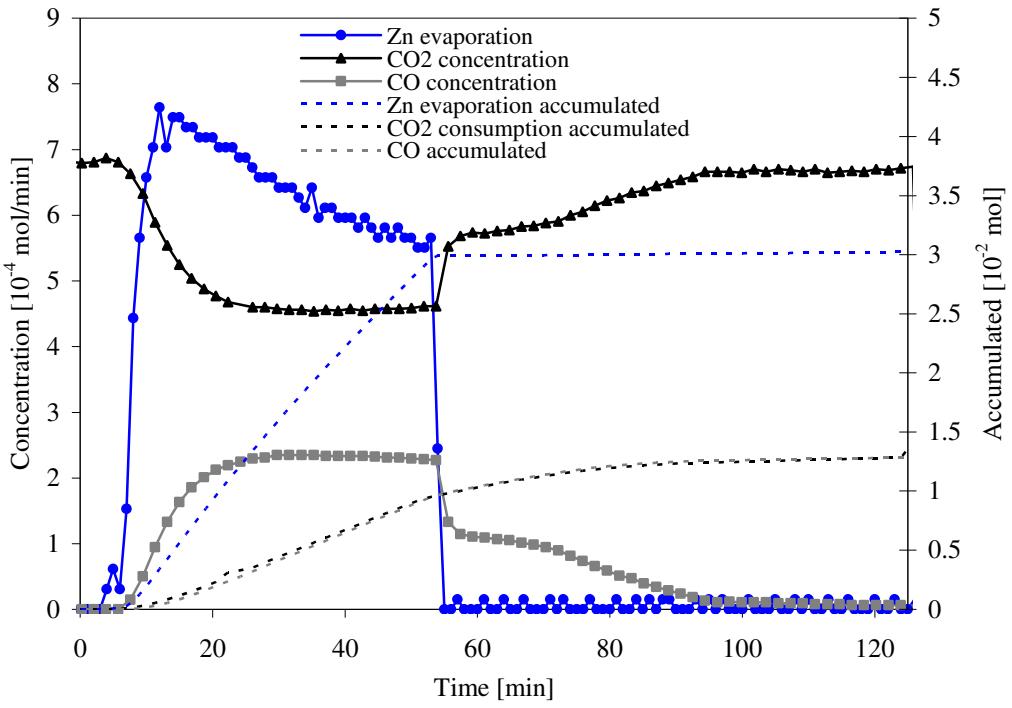


Fig. 8-3: Zn evaporation and gas concentrations in the outlet gas as a function of time during the isothermal oxidation of zinc with a stoichiometric ratio $CO_2$:Zn(g) of 1.06 and reaction zone temperature of 773 K.

## 8.5. Data Acquisition

The performance of the $CO_2$ splitting reactor can be described by the zinc to zinc oxide conversion and the $CO_2$ conversion either to CO or C. Both criteria are important for the successful implementation of the reactor, as high conversion reduces the need for mass recirculation and enhances overall efficiency.

The Zn to ZnO conversion is given by eq. (8.1) where $n_{ZnO}$ is the total number of moles of ZnO produced and $n_{Zn}$ is the total number of moles zinc evaporated during an experiment.

$$X_{Zn} = \frac{n_{ZnO}}{n_{Zn}} \tag{8.1}$$

With the given setup it is only possible to measure the number of moles zinc evaporated but not the number of moles ZnO produced during the experiment. Assuming no production of C and all $CO_2$ consumed is converted to CO, the Zn conversion may be expressed by eq. (8.2).

$$X_{Zn} = \frac{n_{CO}}{n_{Zn}} \tag{8.2}$$

$n_{CO}$ corresponds to the number of moles CO produced, which is measured by the GC. $n_{Zn}$ is the number of moles Zn evaporated during the experiment and measured by the balance.

To check whether C was produced during the experiment and verify the assumption for eq. (8.2), eq. (8.3) was applied.

$$n_C = n_{CO_2,consum} - n_{CO} \tag{8.3}$$

$n_{CO_2,consum}$ corresponds to the number of moles $CO_2$ consumed during the experiment. To estimate the $CO_2$ conversion, again assuming no production of C, eq. (8.4) is applied:

$$X_{CO_2} = \frac{n_{CO}^t}{n_{CO_2}^t} \tag{8.4}$$

$n_{CO}^t$ corresponds thereby to the number of moles CO produced and $n_{CO_2}^t$ to the total number of moles $CO_2$ introduced to the reactor during time t. The $CO_2$ conversion was believed to be most representative for time t accounting for the linear part of the reaction during the evaporation of zinc (see Fig. 8-3). Taking into account the $CO_2$ introduced after time t would reduce the $CO_2$ conversion drastically and not be representative.

To judge how much of the zinc introduced to the reactor is collected on the filter, the particle yield is calculated by eq. (8.5), where $m_{Filter}$ is the total mass deposited on the filter at the end of the experiment and $m_{Zn,crucible}$ is the total amount of zinc initially put into the crucible.

$$Y = \frac{m_{Filter}}{m_{Zn,crucible}} \tag{8.5}$$

## 8.6. Results and Discussion

In Fig. 8-4 the accumulated CO production is plotted as a function of time for various $CO_2$:Zn stoichiometries while all other parameters were kept constant. The dotted line is representing the time during which Zn evaporation took place. During Zn evaporation the accumulated CO production follows a linear trend signifying a chemical reaction controlled process. While for experiments carried out at high stoichiometries the CO evolution immediately stops once Zn evaporation comes to an end, an ongoing oxidation can be observed for experiments carried out with lower stoichiometries. The CO production then follows a parabolic rate law indicating diffusion controlled processes. Furthermore, with increasing stoichiometry an increase in CO production rate can be observed. Consequently the highest Zn conversion of 91% was found for the experiment with a stoichiometry of 32.42.

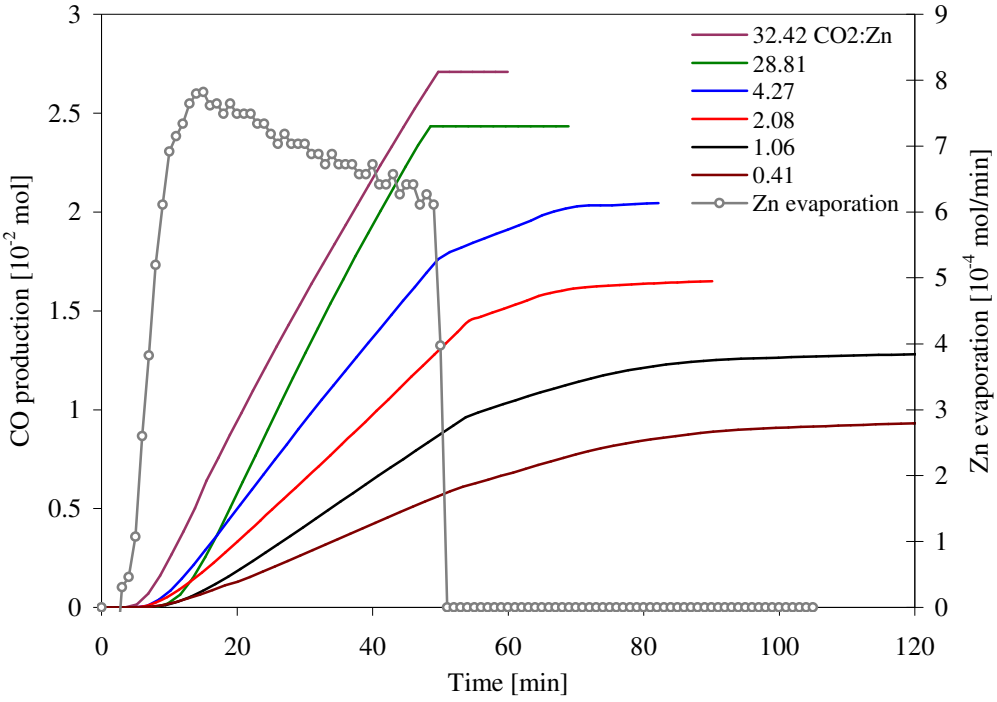


Fig. 8-4: CO production as a function of time for various CO2:Zn(g) stoichiometries in the range of 0.41-32.42. The Zn evaporation was kept constant for all experiments and is exemplary given by the dotted line.

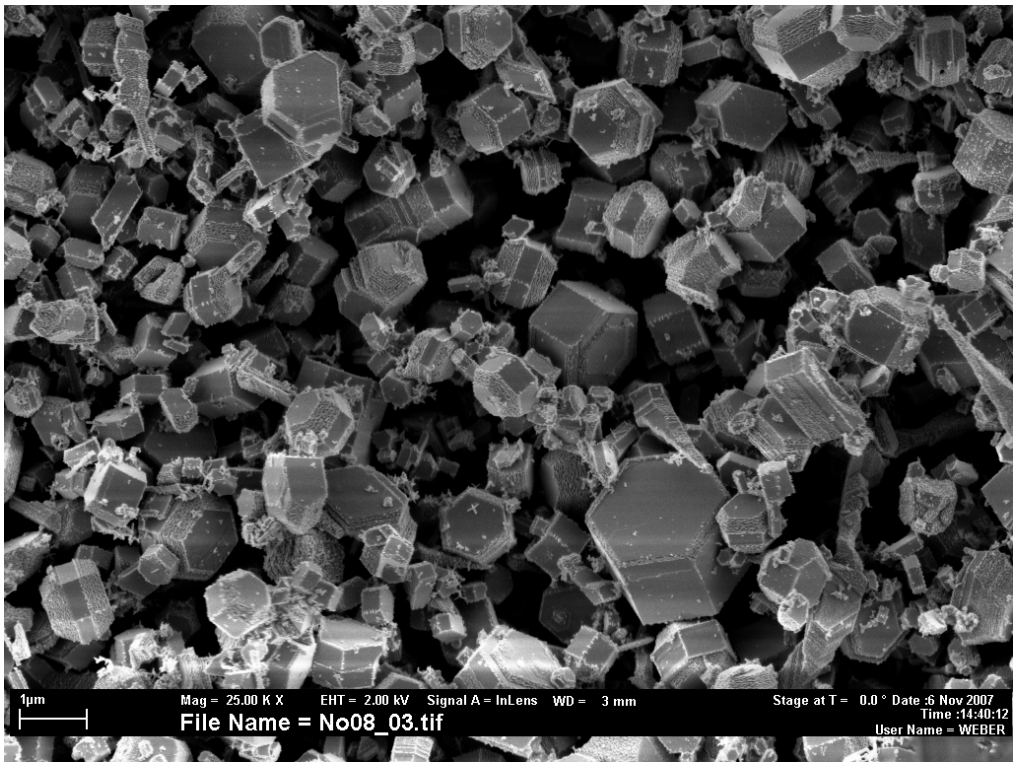


Fig. 8-5: SEM picture of Zn particles deposited on the filter ($CO_2$:Zn(g) = 0.41, XRD: 100% Zn)

SEM pictures of samples taken from the filter (Fig. 8-5) and from the reaction zone (Fig. 8-6) revealed that two different mechanism took place: A part of the Zn vapour formed hard solid deposits on the reactor walls whereas on the filter hexagon-based rods and drums with truncated edges have been found. According to Ernst et al. [43] sharp-edged particles as found on the filter are formed by Zn supersaturation in the cooling zone. However with the minimum cooling zone temperature of 760 K it is not clear whether particle formation took place before the reaction zone. Depending on the particle formation mechanism, heterogeneous or homogenous nucleation, the probability for particle formation requires different saturation ratios [46]. From a theoretical point of view it is therefore difficult to determine the formation of particles. Hence, to identify distinctly the location of particle formation it would be necessary to remove samples at different positions during the reaction, which is not possible with the given setup.

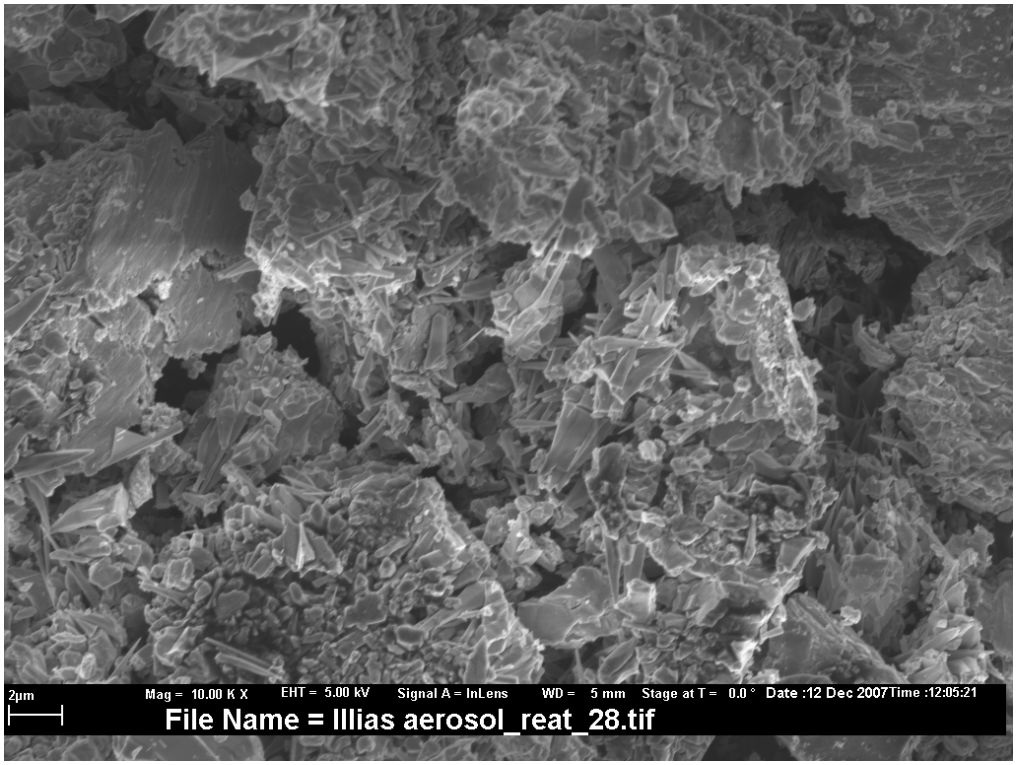


Fig. 8-6: SEM picture of ZnO deposits in the reaction zone ($CO_2$:Zn(g) = 4.27, XRD: 100% ZnO)

XRD measurements revealed that the hard solid deposits taken from the reaction zone consist of 100% ZnO while the hexagonal drums collected from the filter consist of 100% Zn. Exemplary XRD patterns are given for an experiment carried out at a low stoichiometry of 0.41 (Fig. 8-7) and at high stoichiometry of 4.27 (Fig. 8-8). The gray and black lines represent the samples found in the reaction zone and on the filter, respectively. The characteristic peaks are marked for Zn and ZnO. The fact that the particles collected on the filter consist of pure Zn implies that they either might be formed after the reaction zone or that the residence time in the reaction zone of ~5 seconds is too short for a considerable Zn oxidation. However, even on the surface of the particles, which was studied by photoelectron spectroscopy (XPS, Escalab 220i XL) no evidence for Zn oxidation has been found. The surface compositions for two selected samples and a reference sample (commercial

Zn dust) are given in Tab. 8-1 in terms of atom percentages for the elements C, O and Zn. Both samples show less oxygen percentage than the reference sample indicating that the particles are pure Zn with a natural oxide film. The C percentage occurs from natural impurities when transporting the samples in air.

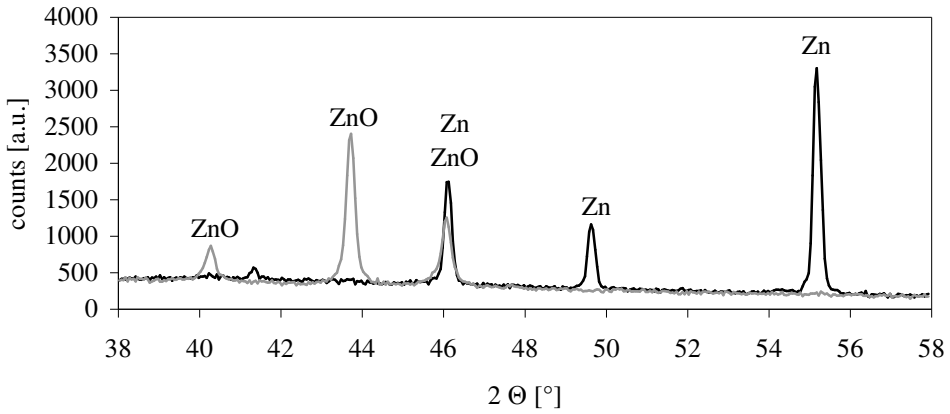


Fig. 8-7: XRD patterns of samples collected from the reaction zone (grey line) and filter (black line) after an experiment carried out with a $CO_2$:Zn(g) stoichiometry of 0.41

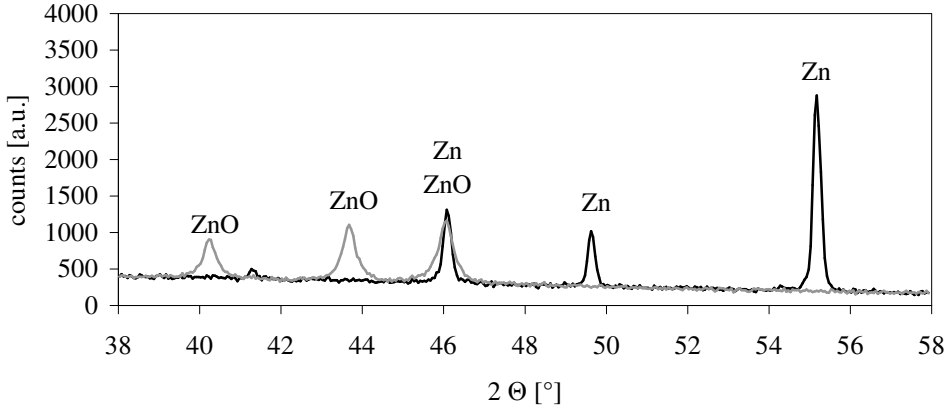


Fig. 8-8: XRD patterns of samples collected from the reaction zone (grey line) and filter (black line) after an experiment carried out with a $CO_2$:Zn(g) stoichiometry of 4.27

| Sample | C | O | Zn |
|---|---|---|---|
| commercial Zn dust (Sigma-Aldrich) | 66.86 % | 27.27 % | 5.86 % |
| stoichiometry 0.41 | 72.3 % | 21.52 % | 6.18 % |
| stoichiometry 32.42 | 73.6 % | 20.79 % | 5.61 % |

Tab. 8-1: Atom percentages on the particle surface of two samples collected from the filter ($CO_2$:Zn(g) stoichiometry of 0.41 and 32.42) and of commercial Zn dust measured by XPS.

Zn conversion, $CO_2$ conversion and particle yield are plotted as a function of stoichiometry in Fig. 8-9. A high stoichiometry, i.e. an excess of $CO_2$, yields to a high Zn conversion and a low $CO_2$ conversion. As seen in Fig. 8-4 a high stoichiometry leads to immediate conversion of Zn on the reactor wall through a chemical reaction controlled mechanism. At a low stoichiometry, e.g. below 1, zinc vapour is in excess and only a part of it is oxidised while the rest is depositing on the reactor walls and filter. Zn deposits on the walls near or in the reaction zone are partly oxidised by diffusion controlled processes and responsible for ongoing CO production after Zn evaporation has stopped. During the time where Zn evaporation takes place, this consequently results in a lower zinc conversion but to an increase in $CO_2$ conversion. The optimum for both, Zn conversion and $CO_2$ conversion is reached at a stoichiometry of 1 with a conversion of 39%.

The particle yield is a relative index only as most particles are depositing between the reaction zone and the filter. Re-positioning of the filter just above the reaction zone would strongly increase the particle yield and shift the curve upwards. However, it can be stated that the measured particle yields decrease with higher stoichiometries. As more Zn is reacting and converted to solid ZnO-deposits on the reactor walls, there will be less Zn (as vapour or as particles) which is able to travel upwards to the filter.

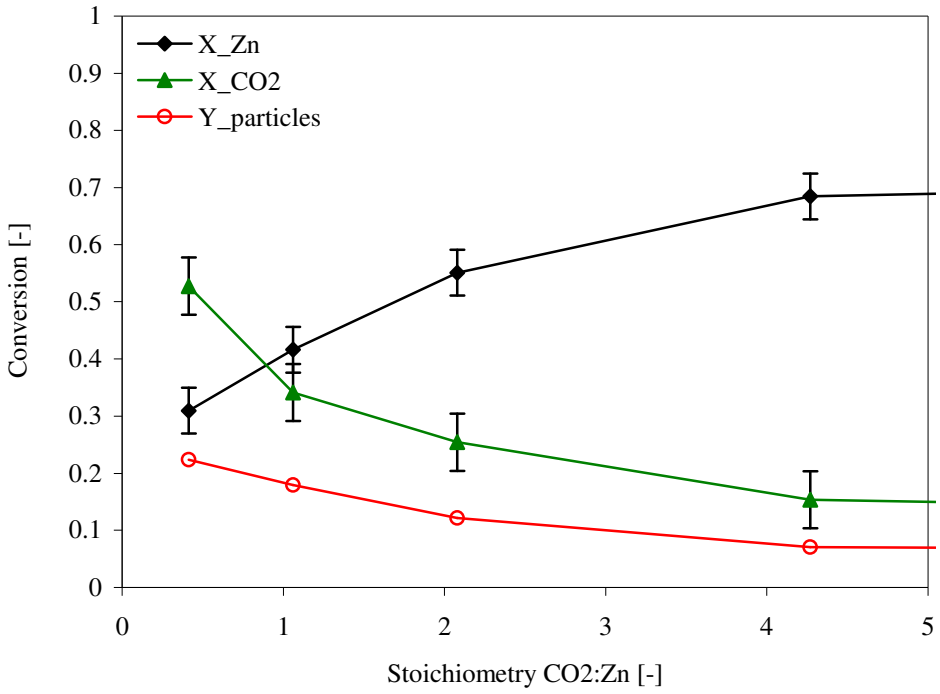


Fig. 8-9: Zn conversion, CO2 conversion and particle yield on the filter as a function of the stoichiometry CO2:Zn(g) in the reaction zone.

The experimental results have shown that reduction of $CO_2$ to CO is well possible at ambient pressure. To investigate whether it is possible to reduce CO further to solid C, three experiments have been carried out in the aerosol reactor using CO as reducing agent at a reaction zone temperature of 773, 973 and 1173 K. The evaporation zone temperature was set to 1173 K resulting

in a Zn concentration of ~$1.5 \cdot 10^{-3}$ mol/min. A CO flow of 0.5 L/min, corresponding to a CO:Zn(g) stoichiometry of ~15, was introduced to the reaction zone. However, in all trials the CO concentration was stable throughout the experiments and no consumption of CO was registered indicating that no reaction takes place under the set conditions. In agreement to Cox and Fray [13] it is believed that Zn is not a viable reducing species for CO at ambient pressure. It is hence not possible to reduce $CO_2$ completely to carbon with Zn at ambient pressure and within a reasonable time scale.

## 8.7. Proposal for a new reactor design

The results from the aerosol reactor have shown that most Zn vapour deposit on the reactor walls where it is subsequently oxidized to ZnO. The oxidation of Zn particles did not take place either due to a low residence time in the reaction zone or because particles were not formed as expected in the cooling zone. To ensure formation of particles before the reaction zone a more intense cooling within the cooling zone should be provided (lower minimum temperature and higher quench rates). A device for doing so was designed and tested by Piatkowski [46]. However, for efficient quenching high gas flows (10-20 L/min) are necessary which will increase costs and decrease exergy efficiency of the reactor (heat loss, gas separation).

The TG study revealed that at intermediate temperatures (673 – 823 K) depending on $CO_2$ partial pressure hollow ZnO cages are formed. Similar to nanoparticles they provide an increase in available reaction surface. By controlling the temperature below the Zn boiling point (1180 K) Zn atoms are sublimated and subsequently oxidised on the previously formed ZnO shell (see Fig. 7-18). To make use of this reaction mechanism a rotary counter flow reactor is proposed. A schematic of the reactor is shown in Fig. 8-10.

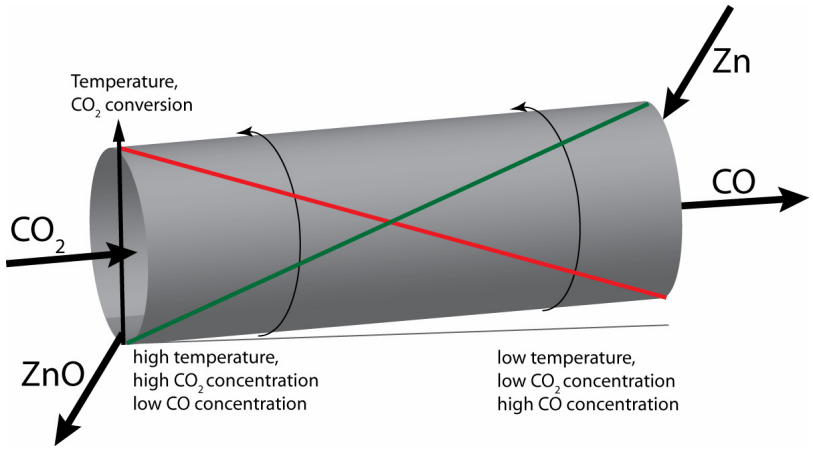


Fig. 8-10: Schematic of a rotary counter flow reactor for the effective conversion of $CO_2$ to CO using Zn as reducing agent.

In the proposed reactor Zn is introduced at one end and $CO_2$ at the other end. The counter flow allows independent maximization of both, Zn conversion and $CO_2$ conversion. By rotating and sloping the reactor, the Zn particles are moved forward and the residence time can be easily

adjusted up to several hours. Furthermore rotation will continuously move and mix the Zn/ZnO bed and prevent sintering of particles. While the reactant gas is flowing through the reactor, the continuous increase in $CO_2$ conversion (from left to right) will lead to an increase of CO and to lower $CO_2$ partial pressures. As observed in the TG experiments, lower $CO_2$ partial pressures allow operating the reactor at lower temperatures and hence a decreasing temperature profile as marked in Fig. 8-10 is suggested.

The advantages over the aerosol reactor are that there is no more need to evaporate Zn. This leads to a reduction of the maximum temperature, saving energy and reducing material restrictions. By immediate oxidation of evaporated Zn on the ZnO shells, Zn(g) diffusion and deposits on the reactor walls can be minimized. There is further no more need for nanoparticles and high quench rates which facilitates handling, saves energy and allows better use of reaction heat. As the reaction will be rather slow with residence times in the order of 30 - 100 min, the use of heat exchanger to recover sensible and latent heat will be facilitated.

A simulation of a finite amount of Zn moving through the proposed reactor and experiencing a steady increase in $CO_2$ partial pressure and temperature has been performed in the TG. The $CO_2$ partial pressure was steadily increased from 0 to 0.9 bar corresponding to a concentration of $6 \cdot 10^{-3}$ mol/min in the outlet gas. The temperature was continuously increased from 635 to 973 K with a heating range of 5 K/min and then kept constant at 973 K for another 40 min. The results, shown in Fig. 8-11, reveal a Zn conversion of 90% which is confirmed by the amount of CO produced. A similar $CO_2$ conversion is expected for the proposed rotary counter flow reactor if enough moles of Zn are fed to the reactor i.e. the same molar amount as $CO_2$ is introduced.

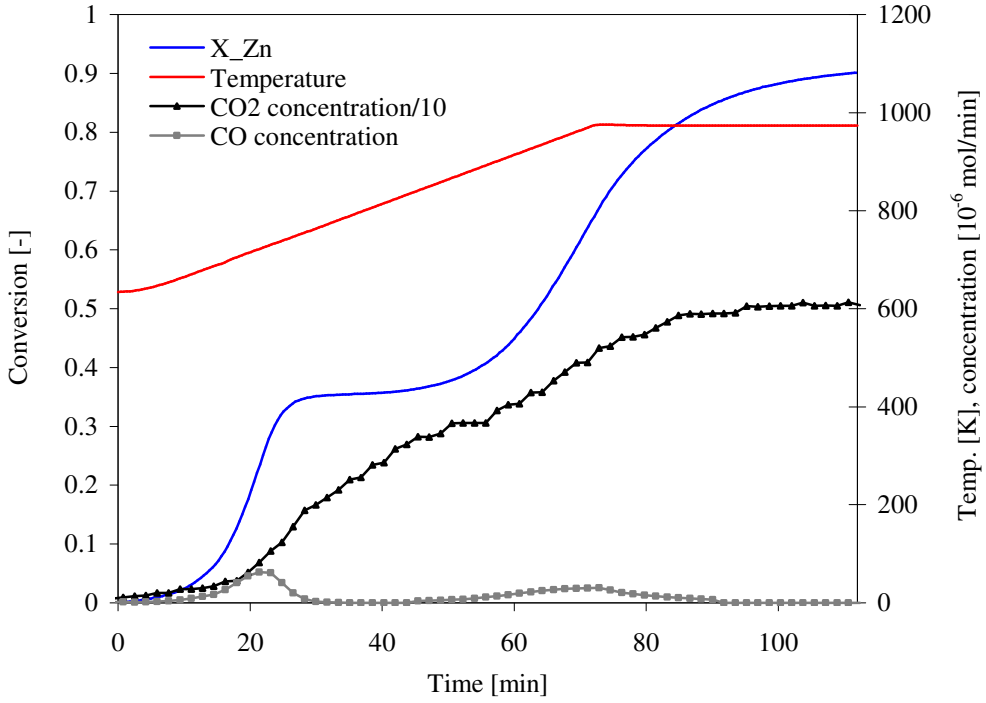


Fig. 8-11: Simulation of a finite zinc sample moving through a rotary kiln, carried out in the TG with various temperatures and $CO_2$ partial pressures.

As in previously performed dynamic runs (see Fig. 7-2), an intermediate decrease of the reaction rate at a temperature of 750 – 850 K can be observed. In agreement to the results obtained in the TG study, an intermediate conversion between 30 – 40 % for lower $CO_2$ partial pressures is reached. While some particles may have cracked and formed hollow ZnO shells, a part of the Zn is enclosed by stronger ZnO layers and unavailable for reaction. The remaining Zn is hence only accessible by extremely slow bulk diffusion through the oxide layer which significantly reduces the reaction rate. A further increase in the temperature forces the sublimation of Zn which is still enclosed by ZnO and leads to an interior Zn overpressure [47]. Once the pressure is high enough the outer ZnO shell cracks and Zn is freely accessible. Surface and gas diffusion processes then allow a faster oxidation and increase the reaction rate again. By going to high enough temperatures, it is possible to reach full Zn conversion through this mechanism. For a proper understanding of the mechanism further studies should be performed concerning the conditions where cracking of particles is favoured. However, for simplicity the reaction could be performed in two successive heating zones. As a first estimate the first heating zone should be around 723 K and the second around 973 K.

# 9 Summary and Conclusions

## 9.1. Summary

A novel $CO_2$ splitting cycle via Zn/ZnO redox reaction has been proposed. Based on concentrated solar power the cycle allows the production of $CO_2$-neutral fossil fuels. A 2nd law analysis revealed that the highest exergy efficiency (solar-to-chemical energy conversion) is obtained by producing CO. A concentration ratio of 10'000 suns yields an exergy efficiency of 39% which exceeds the exergy efficiency for the comparable water-splitting cycle. The use of CO in a combined cycle with an efficiency of 60% gives a solar-to-electricity conversion efficiency of 26%. An economic analysis for the production of solid carbon as sequestration product predicts a rather high unit cost of 416-469 $ per ton $CO_2$ avoided. However, compared to mineral carbonation, the amount of material to be disposed of and the associated environmental impact is reduced by a factor of 10.

A kinetic study of the oxidation of zinc with $CO_2$ has been performed in a thermogravimeter system in the temperature range of 623-823 K. In agreement with previous studies the oxidation of zinc is characterized by two different reaction regimes: a fast initial chemical controlled reaction, where a growing layer of ZnO is formed around the Zn particles, followed by an extremely slow diffusion controlled reaction, where unconverted Zn is completely enclosed by a dense ZnO layer. For the first regime a dependence on $CO_2$ partial pressure of 0.4 has been found. SEM pictures revealed the formation of hollow ZnO shells and formation of ZnO crystals by vapour deposition processes. From the observations the following growth mechanism has been proposed: Oxidation of Zn particle surface leads to a ZnO shell encasing unconverted Zn. At temperatures above 673 K sublimation of Zn inside the ZnO shell leads to an interior overpressure and provokes cracks and holes in the ZnO shell. The formation of cracks enables gas- and surface-diffusion of sublimated and adsorbed Zn atoms and yields higher reaction rates and complete reaction. The formation of cracks is favoured by low $CO_2$ partial pressures or high temperatures e.g. a local temperature increase due to the exothermic conversion. Based on the shrinking core model an apparent activation energy of 96.1-148.1 kJ/mol depending on $CO_2$ partial pressure has been found.

The $CO_2$ splitting with Zn has been studied in an Aerosol flow reactor. Zn has been evaporated and, after passing a cooling zone, brought in contact with the reactant gas, a mixture of $CO_2$ and argon. The mixture then flowed through a reaction zone, heated to 773 K, towards a filter. The highest Zn to ZnO conversion measured was 91%. At a $CO_2$:Zn(g) stoichiometry of 1 an optimum of 39% was found for both, Zn to ZnO conversion and $CO_2$ to CO conversion. The reaction is believed to take place mainly by oxidation of Zn deposits on the reactor walls at intermediate temperatures. As a consequence a low particle yield of 7-22% has been measured and no ZnO was found on the filter.

To make use of the new reaction mechanism resulting in hollow ZnO shells a rotary counter flow reactor has been proposed. Introduction of the reactants in counter flow allows maximization of Zn conversion and $CO_2$ conversion. Operation of the reactor at temperatures between 723 K and 973 K

will lead to complete reaction by immediate conversion of sublimated Zn atoms on the ZnO shell and significantly increase the particle yield.

## 9.2. Conclusion

A promising cycle for the production of solar fossil fuels has been proposed. In combination with $CO_2$ capture it allows unlimited use of the existing fossil fuel based infrastructure and energy conversion technologies. In other words, it makes fossil fuels renewable! For successful implementation of the $CO_2$ splitting in industrial scale, a simple and effective reactor is needed. To do so, the formation of hollow ZnO shells offers a great opportunity for efficient oxidation of Zn and splitting of $CO_2$. The range of temperature will thereby play an important role and has to be chosen carefully in order to provoke cracks for complete oxidation but prevent evaporation and loss of gaseous Zn.

## 9.3. Recommendations for Future Work

- For the production of C it should be first tried to reduce CO with different other metals (e.g. FeO, Mg). A metal able to reduce CO should be capable of reducing $CO_2$ completely to C.

- Using a combination of $CO_2$ and water vapour as reactant gas should allow direct production of syngas. Different $CO_2$ and water vapour concentrations may be studied in the TG in order to produce the "perfect" syngas ($H_2$:CO ratio).

- Further experiments with the TG should be performed to study the precise conditions ($CO_2$ partial pressure, temperature and particle size) for particle cracking and the formation of hollow ZnO shells.

- A novel reactor should be constructed to maximize both, Zn conversion and $CO_2$ conversion and to benefit from the increased reaction surface by the formation of ZnO shells.

- The aerosol reactor may be optimised by eliminating "dead" spaces (remove the outermost quartz tube from the reaction zone), increasing reaction zone length for higher residence times and removing cold reactor walls by decreasing the space between reaction zone and filter. Further experiments may investigate the influence of reaction zone temperature, total mass flow and ratio of reactant gas flow to carrier gas flow.

# 10 Bibliography

[1] Intergovernmental Panel on Climate Change, *IPCC Fourth Assessment: Working Group III Report "Mitigation of Climate Change"*, 2007, www.ipcc.ch

[2] C. Philibert, *Barriers to Technology Diffusion: The Case of Solar Thermal Technologies*, COM/ENV/EPOC/IEA/SLT (2006) 9, http://www.oecd.org/dataoecd/46/14/37671704.pdf

[3] A. Kogan, *Direct solar thermal splitting of water and on-site separation of the products - II. Experimental feasibility study*, Int. J. Hydrogen Energy 23, 89-98, 1998

[4] A. Traynor, R. Jensen, *Direct Solar Reduction of CO2 to Fuel: First Prototype Results*, Ind. Eng. Chem. Res., 41, 1935–1939, 2002

[5] A. Steinfeld, R. Palumbo, *Solar thermochemical process technology*, In: R.A. Meyers Ed., Encyclopedia of physical science and technology, Academic Press, 237-256, 2001

[6] A. Steinfeld, *Solar thermochemical production of hydrogen - a review*, Solar Energy 78, 603-615, 2005

[7] R. Palumbo, J. Lédé, O. Boutin, E. Elorza Ricart, A. Steinfeld, S. Möller, A. Weidenkaff, E. A. Fletcher, J. Bielicki, *The production of Zn from ZnO in a high-temperature solar decomposition quench process - I. The scientific framework for the process*, Chem. Eng. Sci. 53, 2503-2517, 1998

[8] P. Haueter, S. Möller, R. Palumbo, A. Steinfeld, *The production of zinc by thermal dissociation of zinc oxide - Solar chemical reactor design*, Solar Energy 67, 161-167, 1999

[9] Reto Müller, Peter Haeberling, Robert D. Palumbo, *Further advances toward the development of a direct heating solar thermal chemical reactor for the thermal dissociation of ZnO(s)*, Solar Energy 80, 500–511, 2006

[10] C. Wieckert, U. Frommherz, S. Kräupl, E. Guillot, G. Olalde, M. Epstein, S. Santén, T. Osinga, A. Steinfeld, *A 300 kW Solar Chemical Pilot Plant for the Carbothermic Production of Zinc*, J. Sol. Energy Eng., 129, 190-196, 2007

[11] L. R. Martin, *Use of solar energy to reduce carbon dioxide*, Solar Energy 24, 271-277, 1980

[12] L. A. Lewis, A. M. Cameron, *Oxidation Kinetics of Zinc Vapor in CO:$CO_2$ Mixtures: Part I. Comparison with Past Literature*, Metall. Mater. Trans. B 26B, 911-918, 1995

[13] A. Cox, D. J. Fray, *Zinc reoxidation in the shaft of a zinc-lead Imperial Smelting Furnace-1: zinc-carbon-oxygen system with deposition initiated on a quartz substrate and subsequent propagation on zinc oxide*, Trans Instn Min. Metall. (Sect. C: Mineral Process. Extr. Metall.) 109, C97-C104, 2000

[14] K. Ehrensberger, R. Palumbo, C. Larson, A. Steinfeld, *Production of Carbon from Carbon Dioxide with Iron Oxides and High-Temperature Solar Energ*, Ind. Eng. Chem. Res. 36, 645-648, 1997

[15] E. Yamasue, H. Yamaguchi, H. Nakaoku, H. Okumura, K. N. Ishihara, *Carbon dioxide reduction into carbon by mechanically milled wustite*, J Mater Sci 42, 5196-5202, 2007

[16] T. Kodama, M. Tabata, K. Tominga, T. Yoshida, Y. Tamaura, *Decomposition of $CO_2$ and CO into carbon with active wüstite prepared from Zn(II)-bearing ferrite*, J Mater Sci 28, 547-552, 1993

[17] C. Zhang, S. Li, L. Wang, T. Wu, S. Peng, *Studies on the decomposition of carbon dioxide into carbon with oxygen-deficient magnetite I. Preparation, characterization of magnetite, and its activity of decomposing carbon dioxide*, Mater. Chem. Phys. 62, 44-51, 2000

[18] C. Zhang, S. Li, L. Wang, T. Wu, S. Peng, *Studies on the decomposition of carbon dioxide into carbon with oxygen-deficient magnetite II. The effects of properties of magnetite on activity of decomposition $CO_2$ and mechanism of the reaction*, Mater. Chem. Phys. 62, 52-61, 2000

[19] D. Hwang, A. M. Mebel, *Theoretical Study on the Reaction Mechanism of $CO_2$ with Mg*, J. Phys. Chem A 104, 7646-7650, 2000

[20] A. Steinfeld, *Solar hydrogen production via a two-step water-splitting thermochemical cycle based on Zn/ZnO redox reactions*, Int. J. Hydrogen Energy 27, 611-619, 2002

[21] A. Weidenkaff, A. Reller, A. Wokaun, A. Steinfeld, *Thermogravimetric Analysis of the ZnO/Zn Water Splitting Cycle*, Thermochim. Acta 359, 69–75, 2000

[22] S. Möller, R. Palumbo, *Solar thermal decomposition kinetics of ZnO in the temperature range 1950-2400 K*, Chem Eng. Sci. 56, 4505-4515, 2001

[23] A. Roine, *Outokumpu HSC Chemistry® for Windows 5.0,* Outokumpu Research: Pori, Finland, 1997

[24] A. E. Lutz, R. S. Larson, J. O. Keller, *Thermodynamic comparison of fuel cells to the Carnot cycle*, Int J Hydrogen Energy 27, 1103-1111, 2002

[25] C. Song, *Fuel processing for low-temperature and high-temperature fuel cells Challenges, and opportunities for sustainable development in the 21st century*, Catal. Today 77, 17-49, 2002

[26] J. Y. Ren, T. T. Tsotsis, F. N. Egolfopoulos, *Basic Aspects of Combustion Stability and Pollutant Emissions of a CO2 Decomposition-Based Power-Generation Cycle*, Ind. Eng. Chem. Res. 41, 4543-4549, 2002

[27] J. H. Edwards, *Potential sources of $CO_2$ and the options for its large-scale utilisation now and in the future*, Catal. Today 23, 59-66, 1995

[28] A. Yogev, A. Kribus, M. Epstein, A. Kogan, *Solar „Tower-Reflector" Systems: A New Approach for High-Temperature Solar Plants*, Int. J. Hydrogen Energy 23, 239-245, 1998

[29] Intergovernmental Panel on Climate Change. *IPCC Special Report on Carbon Dioxide Capture and Storage,* Cambridge University Press, New York, USA 2005

[30] K. R. Lawless, *The oxidation of metals*, Rep. Prog. Phys. 37, 231-316, 1974

[31] F. Morin, G. Beranger, P. Lacombe, *Limits of Application for Wagner's Oxidation Theory*, Oxidation of Metals 4, 51, 1972

[32] W. H. J. Vernon, E. I. Akeroyd, E. G. Stroud, *The direct oxidation of zinc*, J. Inst. Metals 65, 301-329, 1939

[33] W. J. Moore, J. K. Lee, *Kinetics of the Formation of Oxide Films on Zinc Foil*, Transactions of the Faraday Society 47, 501-508, 1951

[34] C. D. S. Tuck, M. E. Whitehead, R. E. Smallman, *A fundamental study of the kinetics of zinc oxidation in the temperature range 320-415°C in atmospheres of pure oxygen and oxygen doped with gaseous impurities*, Corrosion Science 21, 5, 333-352, 1981

[35] F. O. Ernst, *Co-Synthesis of $H_2$ and Nanocrystalline ZnO Particles by Zn Aerosol Formation and In-situ Hydrolysis*, Dissertation at Swiss Federal Institute of Technology Zürich, Diss. ETH No. 17272

[36] R. Nakamura, J.-G. Lee, D. Tokozakura, H. Mori, H. Nakajima, *Formation of hollow ZnO through low-temperature oxidation of Zn nanoparticles*, Materials Letters 61, 1060-1063, 2007

[37] P. X. Gao, Z. L. Wang, *Mesoporous Polyhedral Cages and Shells*, J. Am .Chem. Soc. 125, 11299-11305, 2003

[38] K. M. Sulieman, X. Huang, J. Liu, M. Tang, *Controllable synthesis and characterization of hollow-opened ZnO/Zn and solid Zn/ZnO single crystal microspheres*, Nanotechnology 17, 4950-4955, 2006

[39] J. Szekely, N. J. Themelis, *Rate Phenomena in Process Metallurgy*, Wiley, New York, 1971

[40] J. Y. Park, O. Levenspiel, *The Crackling Core Model for the Reaction of Solid Particles*, Chem. Eng. Sci. 30, 1207-1214, 1975

[41] O. Levenspiel, *The Chemical Reactor Omnibook*, Corvallis, Oregon, 1989

[42] K. K. Nanda, A. Maisels, F. E. Kruis, H. Fissan, S. Stappert, *Higher Surface Energy of Free Nanoparticles*, Phys. Rev. Lett. 91, 10, 2003

[43] F. O. Ernst, A. Tricoli, S. E. Pratsinis, A. Steinfeld, *Co-synthesis of $H_2$ and ZnO by In-Situ Zn Aerosol Formation and Hydrolysis*, AIChE J. 52, 3297-3303, 2006

[44] H. Ly, R. Weiss, *Design of an Aerosol Reactor for Hydrogen Production by Oxidation of Zinc with Water: A Preliminary Study*, Diploma Thesis, Swiss Federal Institute of Technology Zurich (ETH), 2004

[45] P. Savi, A. Rusconi, *Development of a Zn-Hydrolysis reactor for H2 production*, Diploma Thesis, Swiss Federal Institute of Technology Zurich (ETH), 2005

[46] N. Piatkowski, *Zn-nanoparticle in-situ hydrolysis for hydrogen production in a high quench rate reactor*, Master Thesis, Swiss Federal Institute of Technology Zurich (ETH), 2007

[47] A. Khan, W. M. Jadwisienczak, M. E. Kordesch, *From Zn microspheres to hollow ZnO microspheres: A simple route to the growth of large scale metallic Zn microspheres and hollow ZnO microspheres*, Physica E 33, 331-335, 2006